Side-chain Engineering on Fluorene-based Hole Transport Materials for Low-cost Perovskite Solar Cells with High Stability

Lappeenranta–Lahti University of Technology LUT

Master's Program in Computational Engineering, Master's Thesis

2022

Alaa Almasri

Examiner(s): Professor Erkki Lähderanta

Associate Professor Paola Vivo

ABSTRACT

Lappeenranta–Lahti University of Technology LUT

LUT School of Engineering Science

Computational Engineering and Technical Physics

Alaa Almasri

Side-chain Engineering on Fluorene-based Hole Transport Materials for Low-cost Perovskite Solar Cells with High Stability

Master's thesis

2022

69 pages, 22 figures, 3 tables, 0 appendices

Examiner(s): Professor Erkki Lähderanta

Associate Professor Paola Vivo

Keywords : perovskite solar cells (PSCs), hole transport materials (HTMs), stability, side-chain engineering, carbazole, triphenylamine (TPA)

This thesis aims to investigate the performance and the stability of standard *n-i-p* mesoscopic perovskite solar cells (PSCs) that employ novel organic hole transport materials (HTMs) with different side chains, such as carbazole (FL01) and triphenylamine (TPA) (FL02), as alternative to the commercially available Spiro-OMeTAD. The aim is to reduce the cost of the HTM while featuring good hole transport capability which, in turn, results in high

performance and enhanced stability of the corresponding HTM-based PSCs. The comprehensive experimental characterizations carried out in the thesis reveal that the FL02 HTM-based PSCs display a high-power conversion efficiency (PCE) of ~18 %, comparable to that of Spiro-OMeTAD HTM-based devices, and a significantly increased photostability in air. These results suggest the potential of this novel design to replace the traditional costly and poorly stable HTMs.

ACKNOWLEDGEMENTS

I want to sincerely thank my parents for their unwavering support in helping me succeed in all of my endeavours throughout my life and they have done more for me than I can ever express. I thank God for blessing me with my lovely parents and such a fantastic opportunity.

This work has been achieved in the Red Labs of the Engineering and Natural Sciences Faculty, Tampere University. As a beginning, I place on record my sincere gratitude to Associate Professor Paola Vivo, who accepted me as a member of Hybrid Solar Cells (HSC) Research group. I had the chance because of her to learn a lot of things in the chemistry lab and write this thesis that she supervised and carefully reviewed.

I would like to express my sincere thanks to Professor Erkki Lähderanta for his supervision and examination of this Thesis.

In the same manner, I would like to extend my gratitude to co-supervisor Dr. Maning Liu at Tampere University. He provided me with a wealth of suggestions, insightful conversations, and constructive criticism. He also encouraged me and guided me in the correct way. He has taught me a lot, and without his assistance, I would not have been able to effectively complete my thesis.

My special thanks and gratitude to my lab mate Basheer Al-Anesi for his supporting and leading me. He helped and taught me a lot of things regarding in chemistry lab, experimental measurements, and data analysing.

I would like to extend my gratitude to all of the faculty and members of the HSC team: Paola Vivo, Maning Liu, Basheer Al-Anesi, Anastasia Matuhina, Noora Lamminen, Paavo Mäkinen, and Murthy Grandhi for their supporting and friendliness.

ALAA ALMASRI

CONTENTS

List of Abbreviations

Au	Gold
BDT	benzoyl[1,2-b:4,5-b']bithiophene
Br	Bromide
C-TiO_2	Compact-Titanium dioxide
CB	conduction band
CBM	conduction band minimum
Cl	Chlorine
Cs	Cesium
$CaTiO_3$	Calcium titanate
DFT	density functional theory
DMF	N,N-dimethylformamide
DMM	digital multimeter
DMSO	dimethyl sulfoxide
DSSC	Dye-sensitized solar cell
EHP	electron-hole pair
ETM	Electron transfer material
FA	Formamidinium
FF	fill factor
FK209	tris(2-(1H-pyrazol-1-yl)-4-tert-butylpyridine)cobalt(III)(bis-trifluoromethylsulfonyl)imide))
FL01	Carbazole
FL02	Triphenylamine (TPA)
FTO	Fluorine-doped Tin Oxide
GaAs	Gallium arsenide
GHG	Greenhouse gas
HCl	hydrochloric acid
HOMO	Highest Occupied Molecular Orbital
HTL	Hole transfer layer
HTM	Hole transfer material
I	Iodide

IR	infrared
ITO	Indium Tin Oxide
J-V	current density-voltage
LCB	lower conduction bandgap
Li-TFSI	bis (trifluoromethane) sulfonimide lithium salt
LUMO	lowest unoccupied molecular orbital
m-TiO_2	Mesopores-Titanium dioxide
MA	Methylammonium
$MAPbBr_3$	Methylammonium lead bromide
$MAPbI_3$	Methylammonium lead iodide
MoO3	molybdenum trioxide
MPPT	maximum power point tracking
NREL	National Renewable Energy Laboratory
O_3	Ozon
OLEDs	organic light-emitting diodes
Pb2	Lead
PCE	Power conversion efficiency
PEDOT: PSS	poly(3,4-ethylenedioxythiophene)-poly (styrenesulfonate)
PL	photoluminescence
PSCs	Perovskite solar cells
PV	Photovoltaic
QDSC	Quantum dot solar cell
SCLC	space-charge-limited current
SFX	Spiro[fluorene-9,9′-xanthene]
Sn2	Tin
Spiro-OMeTAD	2,2',7,7'-Tetrakis[N,N-di(4-methoxyphenyl)amino]-9,9'-spirobifluorene
tBP	4-tert-butylpyridine
TPA	triphenylamine
TiO_2	Titanium dioxide
TW-yr	Terra Watt per year
VB	valence band
VBM	valence band maximum
UV	ultraviolet

1. INTRODUCTION

1.1 Solar Energy

Renewable and clean energy sources are critical to address the compelling energy issues of our times in an environmentally friendly way, i.e., by replacing the traditional fossil fuels. By 2040, renewables will increase their market share threefold compared to 2015 (Figure 1.1.a) [1]. The great potential of the sun as a free, clean, and unlimited energy source puts solar energy in a key position among the other renewable energy sources [2,3]. Nowadays, the world's annual electricity demand reaches up to 20 TW-yr, and the sun can easily meet this demand by providing 23,000 TW-yr solar energy per year [4]. As shown in (Figure 1.1. b), solar energy significantly outperforms the combination of all other renewable energy sources by orders of magnitude.

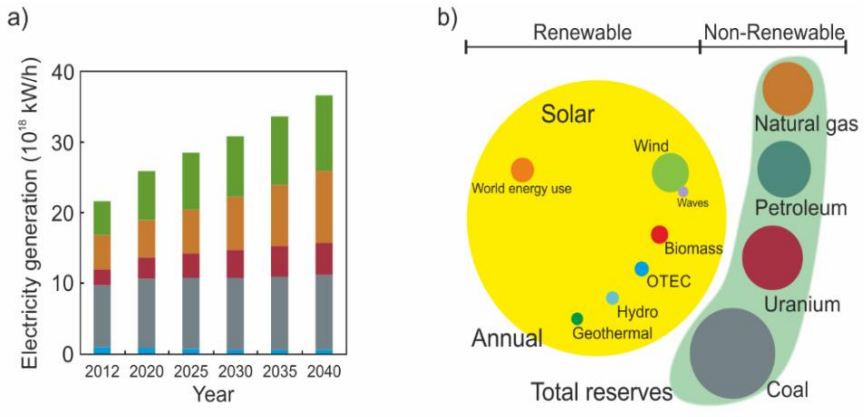

Figure 1.1. a) Electricity generation by various energy sources including liquids (blue), coal (grey), nuclear (pink), natural gas (orange), and world renewables (green). b) Comparison of finite and renewable planetary energy reserves in 2015. Reserves for finite resources are illustrated as total recoverable reserves [1].

Using solar power to produce electricity is an innovative technology that can potentially reduce using finite fossil resources while relieving the global climate change [5]. Presently, the process of converting solar power into electrical energy can be accomplished using solar cells or so-called photovoltaics (PVs) via the photovoltaic effects [2]. The development of efficient solar cells is still a great challenge for the photovoltaic community, especially when

other factors are considered, such as the device stability, processing costs, and technology upscaling from small cells to large modules.

1.2 Development of photovoltaics

The solar cell technologies can be categorized into three generations according to their developmental stages, as depicted in Figure 1.2. Solar cells made of monocrystalline and polycrystalline silicon are often referred to as the first-generation solar cells, which are currently dominating the PV market with an average power conversion efficiency (PCE) of more than 20 % [6,7]. The second generation of solar cells is the thin film solar cells family (including cadmium sulfide, cadmium telluride, copper indium diselenide and amorphous silicon), which consist of layers with thicknesses ranging from nanometers to micrometers. So far, these thin-film based technologies have led to devices with relatively high PCE ~20 % [8]. The third-generation solar cells, also called emerging PVs, have shown great promise due to their low cost, low energy consumption, abundant raw materials as well as the high PCEs achieved [3].

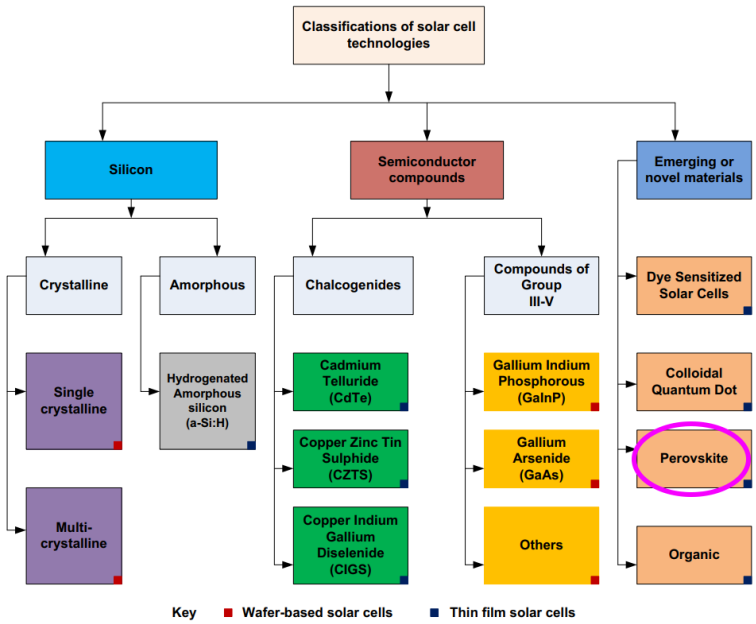

Figure 1.2. Solar cells technologies overview and their current market shares in percent [9].

The emerging PVs generally include polymer solar cell, dye-sensitized solar cell (DSSC), quantum dot solar cell (QDSC), organic–inorganic hybrid solar cells, and Perovskite solar cells (PSCs) [23–25]. In recent years, dye-sensitized solar cells (DSSC), have accomplished the PCE more than 13 % in the laboratory [16].

The tremendous current interest in PSCs stems from the research of the DSSC community. PSCs sparked global excitement due to their exceptional optoelectronic properties, excellent performance in photovoltaics, and low cost of solution-processable fabrication. The first study regarding the organic lead halide compounds methylammonium lead bromide ($MAPbBr_3$) and methylammonium lead iodide ($MAPbI_3$) as sensitizers in DSSCs was disclosed by Kojima et al. [10] They attained a moderate PCE of 3.81 % and 9.7 % with $MAPbI_3$- and $MAPbBr_3$-based devices, respectively. So far, the highest PCE of PSCs has been 25.6 % in 2021, and this efficiency value was certified by the National Renewable Energy Laboratory (NREL) [11]. Figure 1.3 shows the rapid evolution of PSCs' efficiency in the last thirteen years.

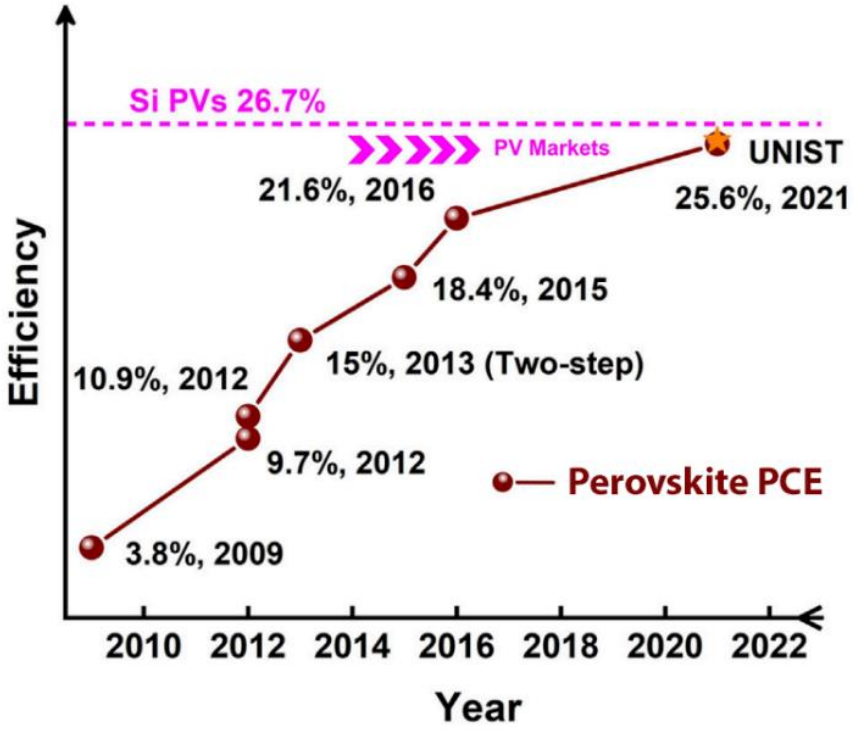

Figure 1.3. The best PCE of PSCs [11].

The PSCs development has been rapid and led to new frontiers of science and technology. Yet, a number of critical factors, such as lead toxicity and device upscaling, could restrict their further development and prevent commercialization [12]. Moreover, the primary challenge with PSCs is the lead halide perovskite semiconductor stability, which is significantly impacted by external environmental factors (e.g., temperature, humidity, and UV radiation) as well as intrinsic factors (e.g., ion migration, perovskite stoichiometry, and bonds strength between cations and anions in the perovskite structure) [13].

Hole transport materials (HTMs) are key constituents of high-performance PSCs and their interface with the perovskite layer has a direct influence on the device performance [14]. Also, the PSCs stability is strongly related to the HTMs hydrophobicity, as most of HTMs are organic materials and need hygroscopic dopants to maximize their charge transport capabilities [15]. The main features of ideal HTMs are an intrinsically high hole mobility, suitable energy levels (Highest Occupied Molecular Orbital (HOMO) level that match with the valence band (VB) of the perovskite layer), long-term stability in air as well as good thermal and photochemical stability [16].

The highest performance (20 % and above) in PSCs has been reached by employing a small-molecule HTM, namely 2,2',7,7'-Tetrakis[N,N-di(4-methoxyphenyl)amino]-9,9'-spirobifluorene (Spiro-OMeTAD). However, the synthesis steps and purification process of Spiro-OMeTAD are tedious and costly and this limits the promising technology commercialization. Importantly, the main reason of the poor stability of PSCs is most probably the oxidized Spiro-OMeTAD exitance as well as dopants, which probably speed up the degradation leading to the decreasing of the device performance [17].

1.3 Aims of the thesis

The purpose of this work is to investigate the performance and the stability of standard PSC structures based on a hybrid triple-cation perovskite (CsFAMA) as the light absorber and novel organic small molecules with carbazole side chains (FL01) and triphenylamine (TPA, FL02) as alternative HTMs to the commercially available Spiro-OMeTAD.

The objectives of this thesis work are

(i) Establish the structure-property-performance relationship for the new HTMs.

(ii) Employ the newly designed TPA (FL02)- and carbazole (FL01)-based HTMs, which combine low-cost with good hole transport property, in CsFAMA-based PSCs.

(iii) Optimize the performance (PCE) of the new HTM-based PSCs and enhance the device stability.

The thesis is organized as follows:

Chapter 2 covers the theoretical background of the research including compositions, crystal structures, and metal halide perovskites optoelectronic properties. In addition, the working operation of PSCs are included, and their constituents (compact and mesoporous Titanium dioxide (TiO_2) based on electron transport materials (ETMs), with a major focus on Spiro-OMeTAD, TPA, and carbazole-based HTMs, and metal electrode (gold)) are introduced. Finally, the stability and cost issues of PSCs are discussed.

Chapter 3 contains the experimental sections explaining in detail the materials used in this work, as well as the various fabrications techniques of *n-i-p* mesoporous PSCs and hole-only structures, which were adopted in the thesis. Finally, the chapter demonstrate the methods of characterization used in this work.

Chapter 4 includes the characterization of the hole mobility, the hole trap density. Photoluminescence (PL) quenching fore relevant samples are discussed. Furthermore, chapter 4 presents the key experimental findings with a detailed discussion on the performance and stability of the fabricated PSCs.

Chapter 5 concludes the thesis and future prospects are outlined.

2. BACKGROUND

2.1 Crystal structure of metal halide perovskites

Calcium titanate ($CaTiO_3$) is an inorganic mineral with a unique crystal structure, namely perovskite. Generally, perovskites are crystalline compounds with a 3D cubic symmetry and ABX_3 stoichiometry shown in Figure 2.1. The perovskite materials used in the solar cells are usually a type of organic-inorganic or fully inorganic metal halides with ABX_3 composition. In the unit cell, A and B sites correspond to positively charged cations of various sizes. A is a large cation, typically a monovalent inorganic/organic cation (Cs^+ (Cesium), MA^+ (methylammonium), or FA^+ (formamidinium)), which is positioned in the vertex of the face-centered cubic lattice enclosed by twelve X-anions. The B cation is a divalent metal ion ($Pb2^+$ (Lead), $Sn2^+$ (Tin)), which is positioned at the body center enclosed by six X-anions. The halogen anion X (Cl^- (Chlorine), Br^- (Bromide), or I^- (Iodide)) occupies the top of the octahedron at the face centers. By using negatively charged X anions, the three-dimensional network structure can be stabilized while fulfilling the charge neutrality requirements. The cubic arrangement consists of BX_6 octahedra sharing the corner edges.

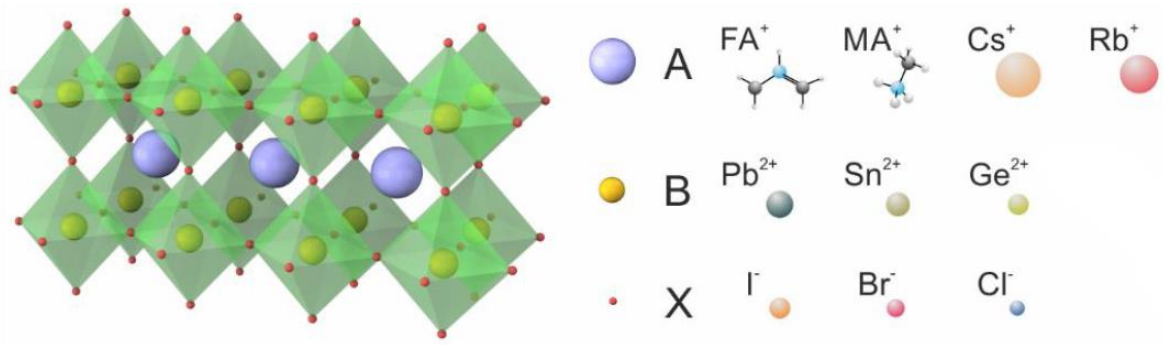

Figure 2.1 3D ABX_3 perovskite structure with the typical constituents at the various sites (A, B, X) of the structure [1].

There has been a significant attention and interest in the perovskite structure because its compositional flexibility enables diverse combinations at the A-site, B-site, and X-site, or even at all three sites simultaneously upon the mixing of different cation or anion, in turn leading to various optical and electronic properties.

2.2 Photovoltaic effect

The solar energy is composed of particles called photons. Depending on the wavelength in the solar spectrum, these photons contain varying amounts of energy. When a certain semiconductor material is exposed to the sunlight, electric current is generated once the energy of incident light is high enough to excite the semiconductor. This process is called photovoltaic (PV) effect. Thus, the PV effect occurs if there is a match between the photon's energy and the so-called bandgap (E_g) of the semiconductor materials. The E_g of the semiconductor is known as the minimum energy amount needed to excite an electron to a free state where it can conduct. E_g corresponds to the energy difference between the lower energy level valence band (VB or E_v), or the highest occupied molecular orbital (HOMO) gap, and the energy level in which an electron may be regarded as free. i.e., the conduction band (CB or E_c) or lowest unoccupied molecular orbital (LUMO). As a result, the bandgap is the minimal energy change needed to excite the electron to be able participating in conduction.

When the sunlight hits the solar cell surface, the photons are absorbed, transferring energy to the free charge carriers. The electrons are excited from the VB/HOMO to the CB/LUMO moving freely in the semiconductor material and participating in conduction. In meanwhile the holes are created in the VB/HOMO. The electrical current is generated accordingly due to the charge carriers' movement with the help of an external circuit.

2.3 Metal halide perovskites optoelectronic properties

2.3.1 Bandgap Tunability

A semiconductor material absorbs of photons when the solar radiation hits the material surface according on the material electronic properties, such as the bandgap and its magnitude. One of the most distinctive merits of the perovskite materials is their tunable bandgap. Upon tailoring of the perovskite material composition, its bandgap can be tuned widely to cover the entire solar spectrum from ultraviolet (UV) to near infrared (IR). Figure 2.2 shows energy level diagram for various perovskite materials

Organic/inorganic metal halide perovskites have generally direct bandgaps. The valence band maximum (VBM) is formed by an antibonding combination of metal s-orbitals and alide p-orbitals, while the conduction band minimum (CBM) is formed by a less anti-bonding integration and more non-bonding p-orbitals of the metal and halide [18]. The VBM energy increases more than the CBM energy when the distance between metal (B-site) and halogen (X-site) is reduced (substitution or phase change) [19].

$CH_3NH_3PbI_3$ ($MAPbI_3$) is a standard perovskite absorber in PV cells, exhibiting excellent charge carrier mobility, making it a rare intrinsic semiconductor [20]. Although the bandgap of $MAPbI_3$ is ~1.55 eV, the absorption wavelength (limited to 800 nm) is not sufficient to achieve panchromatic absorption.

To effectively tune the bandgap of perovskites, mixed halides are commonly used (mostly I and Br) at the X site. It has been found that $MAPb(I_{1-x}Br_x)_3$ has a bandgap ranging from 1.57 to 2.29 eV [21].

For instance, the bandgaps of $MAPbX_3$ show a tunable bandgap from 1.3 eV to 2.3 eV based on the density functional theory (DFT) calculations, where the calculated bandgap values are in good agreement with the experimental ones (Experimental values can be found in the paper [22]).

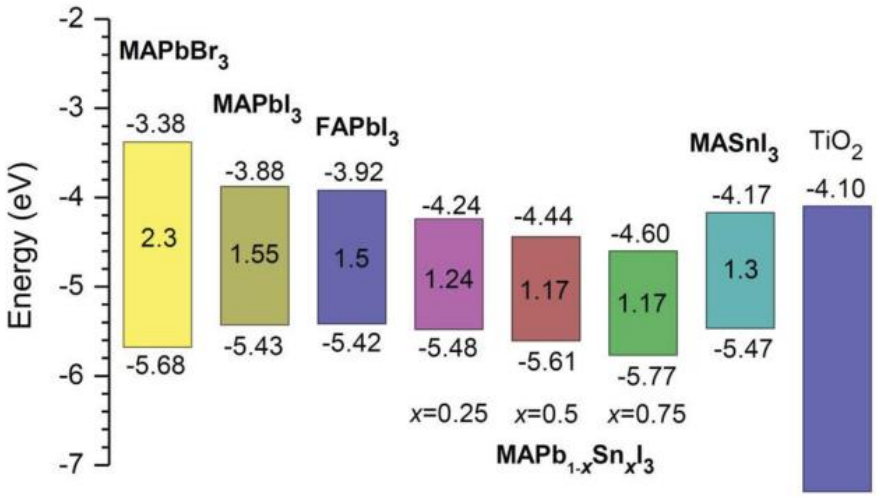

Figure 2.2. Energy level diagrams of $MAPbBr_3$, $MAPbI_3$, $FAPbI_3$, $MAPb_{1-x}Sn_xI_3$, and $MASnI_3$ with TiO_2 [23].

2.3.2 Optical absorption

Photons striking the surface of a semiconductor might be reflected, absorbed, or transmitted. Reflection and transmission are typically regarded as losses in PV devices, since the absorption of the photons is necessary for power generation. An absorbed photon can stimulate the jump of an electron from the valence band to the conduction band.

A photon's energy in relation to the semiconductor bandgap can be divided into three cases:*(i)* $\boldsymbol{E_{ph} > E_g}$**,** strong absorption occurs when photons have energies greater than the bandgap; *(ii)* $\boldsymbol{E_{ph} = E_g}$**,** in order to create an electron-hole pair (EHP), the photons should have sufficient energy, at least equal to the bandgap; *(iii)* $\boldsymbol{E_{ph} < E_g}$**,** the semiconductor transmits photons with low energy compared to the bandgap.

The charge carriers are generated by the photon's absorption in the active layer, when electrons are excited in the semiconductor from the VB/HOMO to the CB/LUMO. If the photon energy is substantially higher than the bandgap, the excited electron is able to release the surplus energy to achieve thermal equilibrium, and these electrons quickly cool down to the conduction band minimum, as illustrated in Figure 2.3. $\boldsymbol{E_C}$ indicates the CBM and $\boldsymbol{E_V}$ represents the VBM.

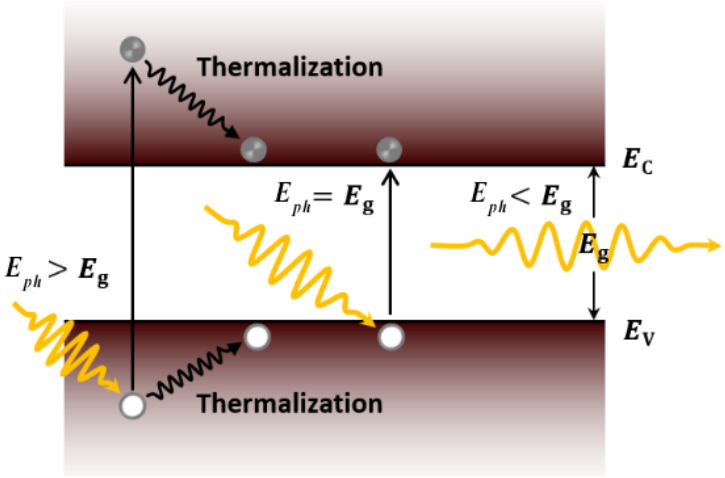

Figure 2.3. The thermalization process [19].

Figure 2.4. illustrates how first and second-generation, and perovskite-based absorbers absorb light optically.

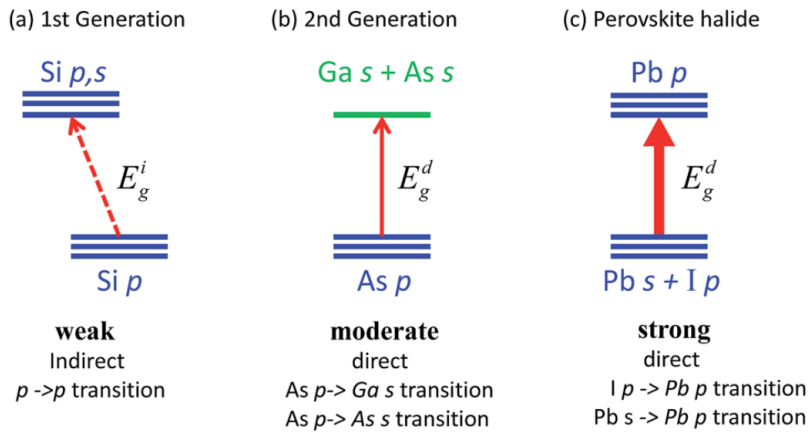

Figure 2.4. Si, GaAs, and Perovskite halide optical absorption [24].

Due to indirect bandgaps, there are no transitions between the band edges for the first-generation absorber (silicon) [24]. The second-generation and third-generation absorbers, such as GaAs and metal halide perovskites, have direct bandgaps, hence their optical absorption is substantially greater compared to silicon.

$MAPbI_3$ and GaAs possess different electronic structures. The VBM in $MAPbI_3$ has been predicted to be mostly made of the s-antibonding states of Pb 6*s* and I 5*p* orbitals, whereas the CBM is primarily made up of the s-antibonding states of orbitals of Pb 6*p* and I 5*s*. The VB orbitals are strongly coupled to Pb lone-pair $6s^2$ and I 5*p* orbitals in this case. GaAs, on the other hand, forms its VB and CB from *p* and *s* orbitals [22]. CBs in GaAs and $MAPbI_3$ have different lower parts, as Ga 4*s* states dominate the lower conduction bandgap (LCB) in GaAs, whereas Pb 6*p* bands dominate in $MAPbI_3$, which have fewer dispersive states than *s* orbitals. As a result, the perovskites exhibit high optical absorption.

2.4 Solar cell parameters

2.4.1 Short-circuit current density

The short-circuit current I_{sc} is the current passing through a solar cell when no voltage is applied on it. The I_{sc} results from the generation and collection of photo-generated charge carriers. There are several factors involved in determining I_{sc}, such as the photon quantity, spectrum of the incident light, and optical properties. I_{sc} is dependent on the solar cell area.

Typically, the maximum current generated by a solar cell is expressed as the short-circuit current density (J_{sc} in mA/cm^2) to incorporate the dependency on the solar cell area.

2.4.2 Open-circuit voltage

The open-circuit voltage, V_{oc}, is the maximum voltage which could be produced from a solar cell, when no current flows through the external circuit. The V_{oc} represents how much the forward bias amount is required to compensate the photocurrent density for the dark current density. V_{oc} is reliant on the saturation current density of the solar cell as well as the photo-generated current.

2.4.3 Fill Factor

The fill factor (*FF*) determines the solar cell maximum power output in incorporation with V_{oc} and I_{sc}. The *FF* represents the ratio between the maximum power ($P_{max} = J_{mp}V_{mp}$) generated by the solar cell and the product of V_{oc} and I_{sc}, and could be represented by the following formula:

$$FF = \frac{J_{mp}V_{mp}}{J_{sc}V_{oc}} \quad (1)$$

where J_{mp} and V_{mp} are the current and voltage, respectively, which the solar cell will produce when operating at the maximum power point. The *FF* represents the squareness of the *I* – *V* curve. The fill factor is expressed as a percentage (%), where higher fill factor means better quality of the solar cells.

2.4.4 Power conversion efficiency (PCE)

Solar cell's PCE is the primary parameter that is used to estimate its performance. Solar cell's PCE is a measure of how efficiently the solar cell can convert the light supplied by the sun to the electricity. Solar cell's PCE is determined by the wavelength and intensity of incident sunlight, as well as the temperature. To fairly evaluate the performance of different

devices, the conditions under which the PCE is assessed must be properly uniformized. In order to characterize the electrical behavior of solar cells and assess their performance, current density-voltage (*J*-*V*) characteristics are recorded under simulated solar irradiation of air mass 1.5 global (AM1.5G, 100 mW cm^{-2}, $T = 25C^{\circ}$).

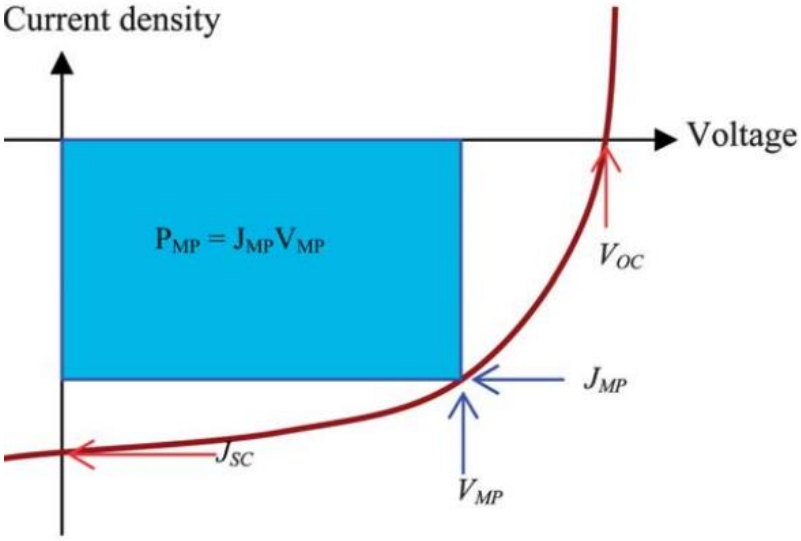

Figure 2.5. $J-V$ characteristics of solar cells under illumination [25].

Figure 2.5. illustrates the current density–voltage $(J-V)$ characteristics of a typical solar cell. From this curve, it is possible to extract the following parameters: the short-circuit current density J_{sc}, the open-circuit voltage V_{oc}, the maximum current density J_{mp}, and the maximum voltage V_{mp} at the maximum power point. According to Equation (2), a device's PCE (also expressed as η), can be calculated as

$$\eta = \frac{P_{max}}{P_{in}} = \frac{J_{mp}V_{mp}}{P_{in}} = \frac{J_{sc}V_{oc}FF}{P_{in}} \quad (2)$$

2.5 Types of metal halide perovskites

2.5.1 Single-cation perovskite

Metal halide perovskite is the heart of PSCs and acts as the light absorber. The $MAPbI_3$-based PSCs have achieved a remarkable performance higher than 20 % [26,27]. Nevertheless, their stability is significantly affected by their exposure to external factors such as oxygen, heat, moisture, and light [28–31]. When switching from a single-halide perovskite such as $MAPbI_3$ to a mixed halide composition (i.e., including Br, Cl, I) a more substantial moisture stability is achieved rather than for the pure iodide. Even though mixed halide perovskites are more stable than iodide-only perovskites, there is a probability that segregation will occur when exposed to continuous light. The reason is that, when the perovskite is in contact with moisture, the H-I bond has lower formation energy than H-Br and H-CI ones, leading to results that Pb-I bonding is broken down in the perovskite crystal structure [32].

The typical formamidinium (FA)-based perovskite, namely $FAPbI_3$, exhibits a lower bandgap (1.47 eV vs. 1.55 eV in $MAPbI_3$) and a red-shifted absorption edge, which are beneficial for higher light absorption and PCEs [33,34].

Using $FAPbI_3$ powder synthesized from less pure lead iodide (PbI_2) precursor, Zhang et al. reported 21.07 % PCE for $FAPbI_3$ solar cells [34]. By means of the powder technique method, the δ phase formation can be prohibited, leading to enhance the device stability

Furthermore, all-inorganic perovskites e.g., $CsPbI_3$ are also utilized in the solar cell applications in spite of their large bandgap (1.73 eV) because they are very stable and can retain the desired photo-active cubic phase even above 300 ℃ [35].

2.5.2 Double-cation perovskite

Mixed A-site occupancy with MA- or FA-cations together with cesium (Cs) results in the hybrid perovskites, which have a stable crystal structure and a widened absorption range due

to the reduced bandgap [36]. CsFA-based double-cation perovskite, e.g., $FA_{0.83}Cs_{0.17}PbI_{0.83}Br_{0.17,}$ has a bandgap of 1.74 eV and good photo-and thermal-stability [37].

Yang. J et al. developed the MA-free (only FA and Cs at the A-site) PSCs that breaks a new PCE record of 21.30 % with a V_{oc} as high as 1.18 V. This is, to date, one of the double-cation PSCs with the highest efficiency [38].

2.5.3 Triple-cation perovskite

The triple-cation system was inspired by the stabilization of α-phase $FAPbI_3$ by MA^+ and Cs^+. The triple-cation perovskite-based PSCs ($Cs_{0.05}(FA_{0.83}MA_{0.17})_{0.95}Pb(I_{0.83}Br_{0.17})_3$, CsFAMA) was developed by Saliba et al [39]. Because of the inorganic cation present in the triple-cation perovskite, its thermal stability and moisture stability are considerably enhanced in comparison to the FA/MA perovskite. CsFAMA is also more resistant to environmental variations, e.g., various preparation protocols, temperatures, and solvent vapors. The environment and stability is crucial for improving the operational durability of PSCs for their large-scale deployment [40].

The CsFAMA perovskite bandgap ranges from 1.6 to 1.76 eV according to the UV-visible and photoluminescence (PL) spectra [41,42]. The CsFAMA film average carrier lifetime is is 304.2 ns [43]. The range of the exciton binding energy is 14– 26 meV according to the Cs concentrations [44].

The CsFAMA-based PSCs exhibit significant improvements in the device stability, as Singh and Miyasaka have confirmed an impressive stability (up to 18 weeks) of triple-cation perovskites fabricated under environmental conditions at a controlled relative humidity of 25-35 % exhibiting a stabilized PCE overwhelming 25 % [45,46]. Table 1 demonstrates a few instances of A-site cation engineering and its effect on PSc performance.

Table 1. Reported representative examples of A-site cation engineering in the solar cells.

Perovskite	Tolerance	Bandgap (eV)	Phase	PCE (%)	References
$MAPbI_3$	0.91	1.55	Tetragonal	21.6	[47]
$FAPbI_3$	0.99	1.47	Trigonal	21.07	[34]
$CsPbI_3$	0.81	1.73	Tetragonal	19.03	[48]
$FA_{0.}1MA_{0.9}PbI_3$	0.92	1.54	Cubic	20.2	[49]
$(FAPbI_3)_{0.92}(MAPbBr_3)_{0.08}$	0.98	1.53	Not reported	23.4	[50]
$(FAPb_3)_{0.95}(MAPbBr_3)_{0.05}$	0.98	1.51	Trigonal	22.7	[51,52]
$FA_{0.9}Cs_{0.1}PbI_3$	0.95	1.52	Cubic	18.9	[53]
$Cs_{0.05}(MA_{0.17}FA_{0.83})_{0.95}Pb(I_{0.83}Br_{0.17})_3$	0.99	1.62	Cubic	21.1	[39]

2.6 Merits of PSCs

PSCs are a rising star in PV technology cells. Metal halide perovskite materials demonstrate unique electronic and optical properties when organic and inorganic ions are mixed in a special composition and crystal structure. These outstanding properties, together with their solution processability and low precursor cost, make them superior to first- and second-generation semiconductors for solar cells. Some of the main merits of halide perovskite materials are summarized as follows:

1. Perovskites possess high optical absorption coefficients ($a > 10^4\ cm^{-1}$). Therefore, the halide perovskites have excellent photo-electric properties [54,55].

2. These materials have a high dielectric constant, allowing electrons and holes to be transported and collected efficiently [56].

3. Electrons and holes could be transferred simultaneously in the length of ~ 100 nm and even more than 1 µm [10,57–59].

4. Thermal and moisture stability can be improved by incorporating inorganic components [32].

5. Organic part can add functional versatility and mechanical flexibility to the device fabrication with cost-effective processes [55].

2.7 Device structures

There are mainly 2 PSC architectures, namely the mesoporous (Figure 2.6 (a)) and planar. The planar can have a standard (*n-i-p*) or inverted (p-i-n) (Figure 2.6 (b), and (c)) configuration, according to the deposition of the perovskite layer on the ETM or HTM, respectively. To achieve high-performance PSCs, a precise control of morphology and crystallization of perovskite as well as appropriate charge transporting materials are pivotal.

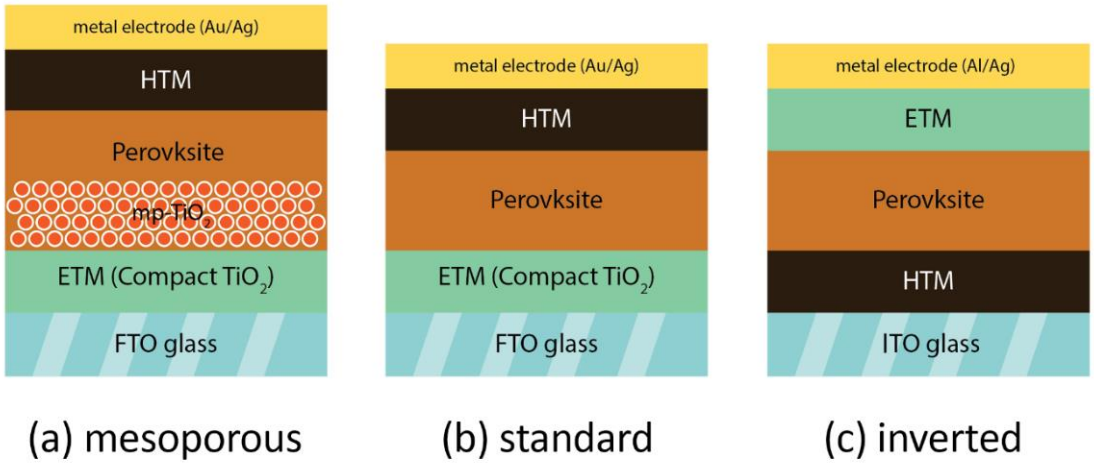

Figure 2.6. Typical PSC architectures: (a) mesoporous, (b) standard planar, and (c) inverted planar.

2.7.1 Mesoporous structure

Numerous studies have been carried out on mesoporous materials (e.g., titanium dioxide, TiO_2) and frequently utilized due to large specific surface area and high porosity. Mesoporous solar cell structure is typically composed of a glass, an electron transport material (ETM), a mesoporous layer, a perovskite layer, a hole transport material (HTM), and a metal electrode layer (Figure 2.6 (a)). In the mesoporous PSC structure, the main function of mesoporous- TiO_2 (m-TiO_2) is to work as a scaffold layer. The m-TiO_2 layer plays a major role in controlling the perovskite materials crystallization as well as in the charge carrier transport [60], especially in extracting and blocking electrons and holes, and preventing recombination EHPs in the Fluorine-doped Tin Oxide (FTO) electrode. As a result, the photoelectric conversion efficiency of the device is improved [13].

The perovskite devices seem to be more efficient when the mesoporous layer in PSCs with an *n-i-p* structure is thinner than 300 nm [21]. Mesoporous structures are currently the most popular and famous structures to fabricate the high-performance PSCs with a PCE above 21 % [61].

Some researchers have also found that the inclusion of a mesoporous layer enhances the device stability in PSCs as well as reduces the $J - V$ hysteresis [12].

2.7.2 Planar structure

Planar structures do not have a porous mesoscopic framework, instead just contain a layered structure. Hence, planar PSCs require minimal configuration and simple fabrication [2]. Depending on the configuration, they are either standard (n-i-p), with an 'FTO|ETM|perovskite|HTM|metal electrode' device configuration, or inverted (p-i-n), with an 'Indium Tin Oxide (ITO)|HTM|perovskite|ETM|metal electrode' device structure.

Among different PSC configurations, the planar structure is relatively simple, particularly for studying charge separation and transport between layers because of the large heterogeneous phase contact [62].

An ETM and an HTM form two interfaces with the perovskites, where the EHP separation takes place. Planar structure enables a straightforward understanding of the light absorption mechanism and the separation of electron-hole. Furthermore, it offers higher device optimization flexibility than the mesoporous counterpart with larger room for developing high-efficiency PSCs in the future [52].

2.8 Perovskites solar cell operation

When light hits a PSC, the perovskite layer absorbs the photons to create excitons. Upon the excitation, free charge carriers (free electrons and holes) can be generated. The ETM and HTM layers collect the dissociated electrons and holes, respectively. The perovskite layer in an *n-i-p* standard device transfers the electrons to the ETM layer (such as TiO_2), which are then collected by the FTO electrode. Simultaneously, the holes are transferred to the HTM layer (such as Spiro-OMeTAD), which are thus collected by the metal electrode (like gold, Au). Afterwards, the external circuit between the FTO and the metal electrode enables the generation of electricity.

According to Marchioro et al., in order to achieve good charge transport, EHPs should efficiently separate at the TiO_2|perovskite and Spiro-OMeTAD|perovskite followed by electrons injecting into TiO_2 (i) and holes injecting into HTM (ii) [63]. In the meanwhile, a series of phenomena that negatively impact the device performance, e.g., exciton annihilation (iii), photoluminescence, or nonradiative recombination, as well as reverse transmission of electrons and holes ((iv) and (v)) and direct recombination at the TiO_2/HTM interface (vi), will also happen. The electrons and holes transport operation in a PSC cell is illustrated in Figure 2.7.

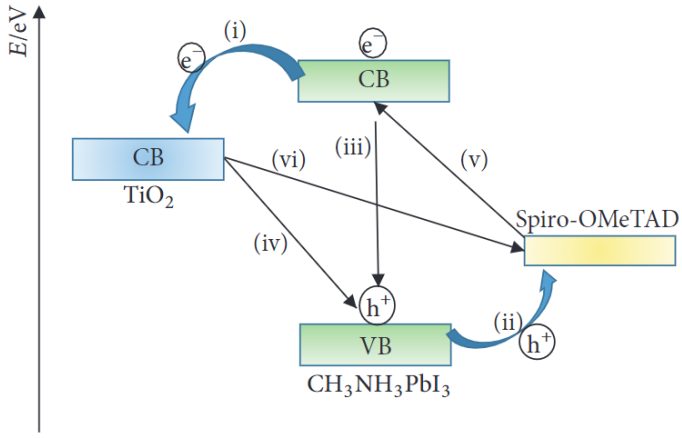

Figure 2.7. Working principle of PSCs [13].

2.9 Conventionally doped HTMs & the alternatives

A key and essential component of PSCs is the HTMs which have gained considerable scientific and technological interests. The primary function of HTM layer is extracting and transporting holes firstly from the perovskite layer through corporation with the ETM layer and then, achieving the separation of the EHPs within the perovskite material. The HTM designing for PSCs needs to enable effective energy level tuning for matching the perovskite's VB and CB edges. This guarantees efficient hole extraction from the perovskite layer and, at the same time, blocks electrons from getting to the top metal electrode [64].

HTMs have a direct influence on the device performance, as they have an important function in the recombination reduction [14]. Also, the PSCs stability relies on the morphology and hydrophobicity of HTMs, yet most of organic HTMs have an acidic hygroscopic nature [15]. A challenge that needs to be addressed urgently is the design of low-cost, efficient, and hydrophobic HTMs that lead to stable PCSs [65,66].

Most of the proposed HTMs are organic small-molecules and polymers. A small molecule has a distinctive weight of structure and molecular, hence it is the best option for industrial production when high purity and yield are required. Conversely, the advantages of polymeric HTMs are that they normally have high hole mobilities without the need of doping, and have a relatively high thermal and mechanical stability [32].

2.9.1 Spiro-OMeTAD

Spiro-OMeTAD is the most common and popular organic small-molecular HTM for high-performance PSCs due to simple deposition methods (solution-processable) and good conductivity [23], as it effectively penetrates in the nanostructure of perovskites [13] and its HOMO is well positioned with respect to the VB of perovskites [13,67].

However, the device based on pristine Spiro-OMeTAD permanently shows low performance due to its intrinsically low hole-mobility (2×10^{-4} $cm^2\cdot V^{-1}\cdot s^{-1}$ [68]) of this HTM. The Spiro-OMeTAD layer hole mobility can be enhanced by doping additives, e.g., bis (trifluoromethane) sulfonimide lithium salt (Li-TFSI) [68]. Typically, tert-butylpyridine (tBP) is also added together with Li-TFSI as tBP enhances its solubility, and thus improves the film's homogeneity. Furthermore, the incorporation of cobalt salts, like tris(2-(1H-pyrazol-1-yl)-4-tert-butylpyridine) cobalt (III)(bis-trifluoromethylsulfonyl)imide)) (FK209), could lead to even higher electrical conductivity. So, the highest PCE of PSCs has been accomplished with doped Spiro-OMeTAD HTMs.

However, the Spiro-OMeTAD synthesis procedures and purification process are tedious and costly (91.67 \$ g^{-1} [69]) and this restricts the large-scale application of this material. The development of low-cost alternative small molecular HTMs has been intensified in order to resolve this issue [70]. The properties of potential HTMs have been systematically linked to different factors, such as alkyl chains [71], molecular planarity [72], three-dimensional (3D) molecular structure [73], molecular size [74], and methoxy groups [75,76]. Researchers have extensively investigated several molecular moieties for HTM designs, including triphenylamine (TPA), triazatruxene, butadiene, and carbazole [66].

2.9.2 TPA-based HTMs

TPA is a non-basic organic compound (unlike most amines) with formula $(C_6H_5)_3N$. The central nitrogen atom of TPA is directly linked to three aromatic groups. The lone pair of nitrogen can attract electrons from any aromatic group acting as an electron acceptor [77]. A partial positive charge will be conferred on nitrogen by the nitrogen lone pair delocalization,

counterbalanced by the partial negative charge at the aromatic site. The electrical conductivity and electroluminescence of TPA derivatives make them useful as hole-transport layers in organic light-emitting diodes (OLEDs) and PVs[78].

TPA-based HTMs are thermally and morphologically stable and possess remarkable charge transport ability. A variety optoelectronic material, e.g., DSSCs and PSCs, have utilized the TPA units as HTMs. The TPA functional moiety exhibits 2 essential characteristics: *(i)* The nitrogen atom of an amine is easily oxidized, *(ii)* TPA can transport positive charges effectively [79,80]. HTMs are found in many aromatic amines, where the electron donating amine nitrogen atom plays an important role [80]. Since the nitrogen atoms contain many electrons, the organic HTMs are often based on TPA moiety, which minimizes the distance of the intermolecular that leads to the non-planarity [32].

Wu et al. studied TPA-based compound composing of benzoyl[1,2-b:4,5-b'] bithiophene (BDT) derivative (BTPA-2), which was employed in $FA_{0.85}MA_{0.15}PbI_3$-based PSCs as the HTM [70]. Their results show that BTPA-1 and BTPA-2-based devices demonstrate the best PCEs of 12.76 % and 13.97 %, respectively, and the latter case has a higher environmental stability than the former [70]. In addition, Zhang et al. developed two HTMs based on Spiro[fluorene-9,9′-xanthene] (SFX)-derived pendant groups, namely X26 and X36. They found that the SFX pendant groups presented in TPA-based molecules significantly affect the conductivity, energy levels, as well as surface morphology of X26 and X36 thin films. X26 HTM in PSCs demonstrates a remarkable PCE of 20.2 %. Moreover, following a period of five months in the condition with regulated humidity (20 %), the X26-based devices still maintained a relatively high PCE of 18.8 % [66].

2.9.3 Carbazole-based HTMs

Carbazole is a heterocyclic aromatic chemical molecule. The chemical structure is made by 2 phenyl rings combined together by two various positions, first connected by a nitrogen atom and second by a Carbon-Carbon bond forming Carbazole tricyclic configuration [81]. This compound has a structure similar to that of an indole, but with a second benzene ring bonded at indole's 2–3 position. Moreover, the aromaticity contributes to the formation of a

fully conjugated orbital along the entire molecule, which in turn leads to the creation of a planar structure along the entire molecule [81]. Therefore, carbazole is typically used as a π-conjugated bridge to construct electron donor–π–electron acceptor organic dyes (D–π–A) [82].

A vast range of applications can be found to utilize the carbazole's electron-rich structure and its ability to donate electrons, whereas it is an ideal candidate for p-donors due to its application diversity. In the organic electronics, carbazole-derived molecules are used mainly as light emitting diodes, dye sensitizers and co-sensitizers in dye-sensitized solar cells, molecular rectifiers in organic semiconductors, and HTMs in PSCs.

There are numerous advantages for carbazole derivatives, including low-cost starting materials, excellent environmental and chemical stability, and strategic sites for attaching functional groups. For instance, a phenylene-derived central core unit was used in Sung et al.'s study of two- or three-arm carbazole-based HTMs [83]. The carbazole-based HTM was almost similar Spiro-OMeTAD-based devices in term of the pCE performance (14.79 and 15.23 %) [83]. An inexpensive carbazole-based conjugated enamine (V950) was synthesized by Daskeviciene et al. by achieving the PCEs of around 18 % [84]. Although the HTMs using a carbazole base have been effectively incorporated into the PSCs, most of them still need doping with lithium and cobalt salts to increase their conductivity, which inhibit stable device-level power output [85].

Coplanarity and interaction of polymer chains are enhanced by the carbazole side chain, while the energy levels and hole mobility are improved. You et al. used carbazole as the conjugated side chain of BDT to create the copolymer PBDB-Cz. PBDB-Cz-based PSCs have a maximum PCE of 22.06 % [86]. Importantly, the PBDB-Cz molecule greatly improved the device stability and, even after 100 days storage at room temperature, the devices still retained more than 90 % of their initial PCEs [86].

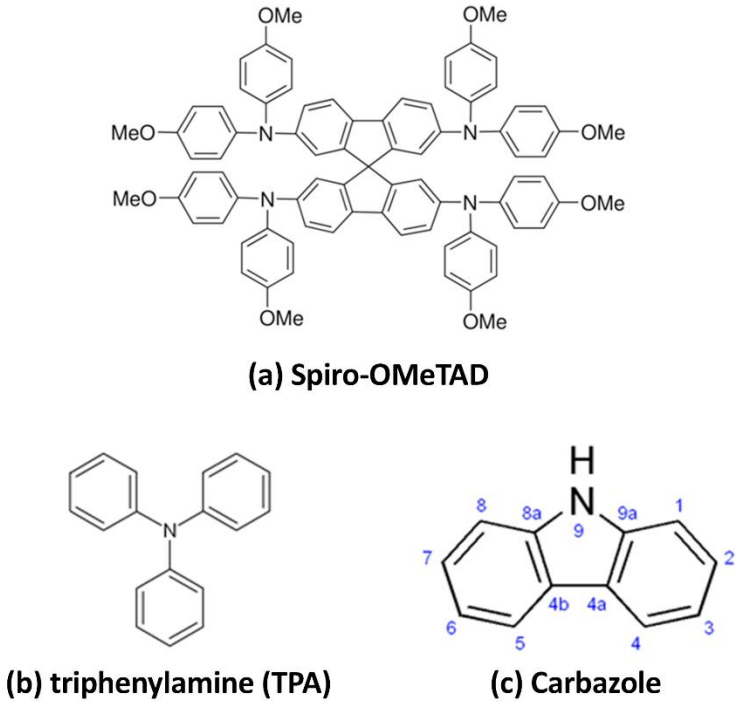

Figure 2.8. Chemical structures of HTMs.

2.10 Stability issue

The low stability of PSCs is one major challenge that limits their practical use. A clear understanding of perovskite degradation mechanisms is still lacking, which will aid in improving the PSCs long-term stability, as a key prerequisite for commercialization. Thus, both intrinsic and extrinsic factors impact on perovskite's long-term stability. It is significant and essential to consider both the internal stability as well as stability under ultimate various external environmental conditions e.g., heat, light, humidity, and oxygen.

2.10.1 External factors

The stability and formability of perovskites can typically be assessed using the Goldschmidt tolerance factor (t), which provides an empirical index of crystal structure prediction of ABX_3. In other words, t determines whether the B-site cation can be accommodated within the octahedral holes of the X-site anion sublattice, as in Equation (3)

$$t = \frac{R_A + R_B}{\sqrt{2(R_B + R_x)}} \quad (3)$$

where R_A, R_B, R_x are the ionic radii of the A-site, B-site, and X-site, respectively. A typical range of organic-nonorganic tolerance is $0.8 < t < 1$ [87].

Perovskite material characteristics are strongly influenced by crystal structure and phase transition. $MAPbI_3$ has a tolerance factor of slightly > 0.9 [88]. Perovskites tend to be structurally stable when a variety of cations and anion are mixed.

Temperature, pressure, and ion radius may influence perovskite phase transition. with a change in temperature, perovskite materials go through different phases. The orthorhombic phase of the perovskite (γ) appears at temperatures lower than 100 K. Temperatures above 160 K lead to the appearance of tetragonal (β) phases instead of the orthorhombic (γ) phases. Higher temperatures around 330 K can induce the formation of another stable cubic phase (α) transition from the tetragonal phase (β) [89,90].

$MAPbI_3$, for example, can be decomposed into PbI_2 and organic iodide (MAI), causing the failure of the corresponding device. It has been monitored that, when perovskite gets exposed to moisture, it produces hydrate products rather than PbI_2 [91]. Another aspect that might impact PSC's function is oxygen. In the presence of oxygen, both charge extraction and transport rates in PSCs drastically decline [92]. However, the doping Spiro-OMeTAD needs an oxidation process to increase its conductivity [93].

UV light possesses a significant impact on the solar cells operation. The photo-generated reactive oxygen species (O_2^-) can promote quick breakdown of perovskites through the deprotonation of MA^+ cations, as well as promote the PSC devices degradation as TiO_2 is also susceptible to UV degradation.

Actually, PSCs are usually degraded by a variety of factors simultaneously, rather than by one particular factor, e.g., oxygen, heat, moisture, and light together. Photo-illumination, oxygen, and heat synergistically accelerate the moisture-induced degradation process [94].

Equations (4)–(7) illustrate the chemical reaction mechanism. When perovskite is in contact with moisture, $CH_3NH_3PbI_3(s) \cdot H_2O$ is broadly formed as an intermediate product in moisture-induced degradation [95,96]. As moisture dissolves $CH_3NH_3PbI_3$, the inorganic halide is left behind.

$$CH_3NH_3PbI_3(s) \cdot H_2O \Leftrightarrow PbI_2(s) + CH_3NH_3I(aq.) \quad (4)$$

Water molecules can still be created by oxygen and photons even in dry air without moisture. Decomposition of perovskite crystals will be accelerated by this process. $CH_3NH_3I(aq.)$ resulting from the perovskite decomposition in the existence of $H2O$ would continue to decompose in ambient to produce $CH_3NH_3I(aq.)$ and $HI(aq.)$ [97]. In other words, the hydrolysis of the organic halide would proceed, releasing HI. As long as moisture exists, organic decomposition is irreversible.

$$CH_3NH_3I(aq.) \Leftrightarrow CH_3NH_3(aq.) + HI(aq.) \quad (5)$$

$$4HI(aq.) + O2 \Leftrightarrow 2I_2(s) + 2H_2O(l) \quad (6)$$

$$2HI(aq.) \Leftrightarrow H_2(g) + I_2(s) \quad (7)$$

Furthermore, continued contact with light causes the perovskite and organic cation to decompose (Equations (8)– (11)).

$$CH_3NH_3PbI_3(s) \Leftrightarrow^{h.v} PbI_2(s) + CH_3NH_2 \uparrow + HI \uparrow \quad (8)$$

$$2I^- \Leftrightarrow I_2 + 2e^- \quad (9)$$

$$3CH_3NH_3^+ \uparrow \Leftrightarrow^{h.v} 3CH_3NH_2 \uparrow + 3H^+ \quad (10)$$

$$I^- + I_2 + 3H^+ + 2e^- \Leftrightarrow 3HI \uparrow \quad (11)$$

Perovskite generally decomposes more slowly when exposed to oxygen. The oxygen in air, on the other hand, has also been shown to cause decomposition in dry and dark conditions [98]. PSCs has been also demonstrating better stability under white light without UV [91].

2.10.2 Degrading from the doped Spiro-OMeTAD HTM

The low stability could be also caused by intrinsic factors, the other components of the solar cell (e.g., HTMs, electrodes and etc.), which lower the quality of perovskites as well as the overall device performance. Because the majority of HTM candidates are organic compounds, e.g., the widely adopted Spiro-OMeTAD-based HTM, the control of annealing temperature is critical, according to the report of Wu et al. [99]. The traditional spin-coating technique enables the formation of Spiro-OMeTAD films with a high macro- and micro-pinholes density. Several studies have suggested that the pinholes in the layer Spiro-OMeTAD may contribute to the degradation of PSCs [100].

The doping Spiro-OMeTAD with additives, such as Li-TFSI, also has a considerable influence on the device performance. Wu et al. [101] demonstrate that low temperature annealing can improve the Spiro-OMeTAD formation and crystallization, however the transfer to the TiO_2 surface and the tBP evaporation, would decrease the voltage potential ofthe device by affecting the Fermi level of the TiO_2. Particularity Li^+ salt could contribute significantly for increasing the Spiro-OMeTAD mobility by two orders of magnitude [102]. The hygroscopic property of Li-TFSI promote its quick transition from solid to liquid once in contact with moisture. Therefore, the devices using Li-TFSI doped Spiro-OMeTAD are quite susceptible to be damaged from the environment with high humidity. In order to substitute Li^+ salts and improve Spiro-OMeTAD's hydrophobicity, great efforts have been made [23,102].

2.11 Cost issue

Although the PSCs efficiencies have increased up to more than 25 % in just a few years, another important consideration for large-scale application is the cost as well as the above-discussed stability (lifetime). PV technologies are evaluated using the golden triangle (Figure. 2.9) including efficiency, cost, and lifetime.

Silicon PVs still accounts for more than 90 % of the present market share of commercialized PVs because it provides a bundle of excellent efficiency of module of 21 %, with more than

25 years lifetime, and cheap cost of 0.3 $ W^{-1} that is closing grid parity. Furthermore, Perovskite lab-scale cells demonstrate the promise due to their high efficiency and low production cost, which is expected to be half that of crystalline Si counterparts [103].

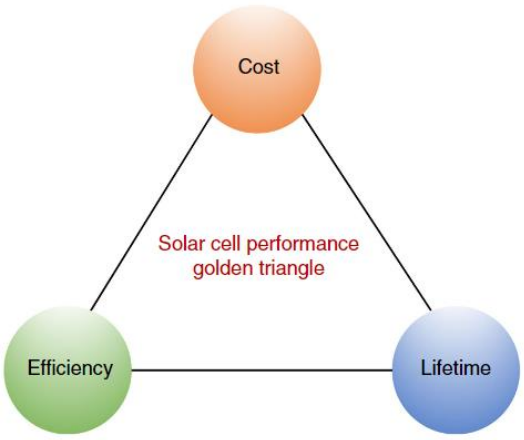

Figure 2.9. Cost, efficiency, and lifetime for the Golden Triangle of solar cells [104]

PSCs have shown impressive performance, particularly with Spiro-OMeTAD, as an effective small molecule HTM. However, the exorbitant price limits its commercial potential.

Hence, for commercial purposes, several researchers are attempting to replace Spiro-OMeTAD with different affordable and effective HTMs that produce devices of PSC with remarkable stability and efficiency. Alternatives to Spiro-OMeTAD have received a lot of attention, particularly small molecule based HTMs, including side chains e.g., TPA and carbazole, which are the main focus of this work.

3 Experimental Details

3.1 Materials

For chemical etching and cleaning of the FTO substrates, the tools and materials are used: big Petri dish, FTO glass (TEC15, 2.2 mm), tape, Zn Powder, HCl, small soft brush, and DMM. For chemical etching and cleaning of the ITO, the tools and materials are used, big Petri dish, ITO glass, tape, HCl, HNO_3, MQW, plastic container, and DMM.

The materials needed for the solar cell fabrication and hole-only device characterization are herein listed as follows: methylammonium bromide (MABr), formamidinium iodide (FAI), and 30 NRD TiO_2 nanoparticle paste. These were obtained from Greatcell Solar Materials. Titanium dioxide (TiO_2), bis(trifluoromethane)sulfonimide lithium salt (Li-TFSI, 99.95 %), dimethyl sulfoxide (DMSO, extra dry, 99.7 %), poly(3,4-ethylenedioxythiophene)-poly (styrenesulfonate) (PEDOT: PSS, 1.3 wt% dispersion in H_2O, conductive grade), molybdenum trioxide (MoO3, 99.97 %), N,N-dimethylformamide (DMF, extra dry, 99.8 %), acetonitrile (99.9 %), chlorobenzene (extra dry, 99.8 %), and 4-tert-butyilpyridine (4-tBP) were obtained from Sigma-Aldrich. Cesium iodide (CsI), $PbBr_2$ (99.999 %) and PbI_2 (99.999 %) were acquired from TCI Europe. Cesium iodide (CsI) was purchased from GmbH. d 2,2′,7,7′-Tetrakis [N,N-di(4-methoxyphenyl) amino]− 9,9′-spirobifluorene (Spiro-OMeTAD, 99 %) were purchased from Lumtec. Tris[2-(1 H-pyrazol-1-yl)− 4-tert-butylpyridine]cobalt(III)tri[bis-(trifluoromethane) sulfonimide] (FK209 Co(III), > 98 %) was obtained from Dyenamo. The materials based on TPA and carbazole are home-made by Prof. Haichang Zhang's group at Qingdao University of Science and Technology (China).

3.2 Fabrication of *n-i-p* mesoporous PSCs

In this work, mesoporous PSCs with standard *n-i-p* structure, consisting of FTO|c-TiO_2|m-TiO_2|CsFAMA|HTM|Au, were fabricated according to an existing protocol [64]. The manufacturing of each layer is described in detail in the following sections, with main focus on the materials, precursors, fabrication procedures, and characterization.

3.2.1 FTO chemical etching

In the above-mentioned solar cell structure, fluorine-doped tin oxide (FTO) coated glass substrates (2 cm × 2 cm) are used as transparent bottom electrodes. The first step is to prepare a 2 M HCl solution with 1 part of concentrated hydrochloric acid (HCl) (37 wt %) and 4 parts of H_2O for etching process. Then, some tape is placed onto one side of the FTO glass to protect part of the substrate according to a customized pattern. The FTO glass substrates are attached inside a Petri dish and covered with zinc (Zn) powder. An as-prepared 2 M HCl solution is poured quickly into the Petri dish, it wets the substrates, and removes the FTO layer from the uncovered parts of the substrates. After waiting for 30s, the etched area of the substrate is wiped away firmly with a small soft brush. After completely wiping the etched area, an excess of sodium bi-carbonate powder is added to stop etching and to neutralize the acid residual. After removing the tape and FTO glass from the Petri dish, the FTO glass is cleaned with a detergent and rinsed thoroughly with distilled water, and finally dried with a nitrogen gun. As a last step, the resistance (expected to be more than 1 M ohm) between the etched and unetched FTO areas is checked with a digital multimeter (DMM).

3.2.2 Substrate cleaning

The glass substrates cleaning is an important step to make sure that the substrates are very pure, dust- and defect-free. The accurate cleaning of the etched FTO substrates should be done by following the below procedure:

1. The substrates are cleaned with 2 % Mucasol solution in water while brushing with a soft brush, then they are rinsed thoroughly with distilled water.
2. The substrates are cleaned by means of ultrasonication with 2 % Mucasol solution in water at 30 °C for 15 minutes, then rinsed with distilled water.
3. Then, they are cleaned by means of ultrasonication with acetone and 2-propanol at 30 °C for 15 minutes, successively.

4. Rinse continuously with acetone and 2-propanol, then completely dry the glasses with a nitrogen gun.

5. Finally, conduct the O_3 & UV treatment for 15 minutes to remove the organic residuals while increasing the hydrophilicity.

3.2.3 Compact TiO_2 layer

A compact TiO_2 (c- TiO_2, ETM) layer is deposited using spray pyrolysis as illustrated in Figure 3.1, following a reported method [105]. The precursor solution is prepared as follows: 2-propanol is added into 3.69 g of titanium diisopropoxide bis(acetylacetonate) stock solution (75 % in 2-propanol) up to 20 mL in total volume (0.38 M final concentration).

Under a nitrogen pressure of 0.12 MPa, the precursor solution is sprayed onto the surface of the glass for 1 s per cycle at a distance of H=14 cm with an alignmentof 40°. Overall, 10 cycles contribute to around 25 nm thickness of compact TiO2 layer, with a 30-second pause between cycles. After coating, the substrate is heated at 450 °C for one hour.

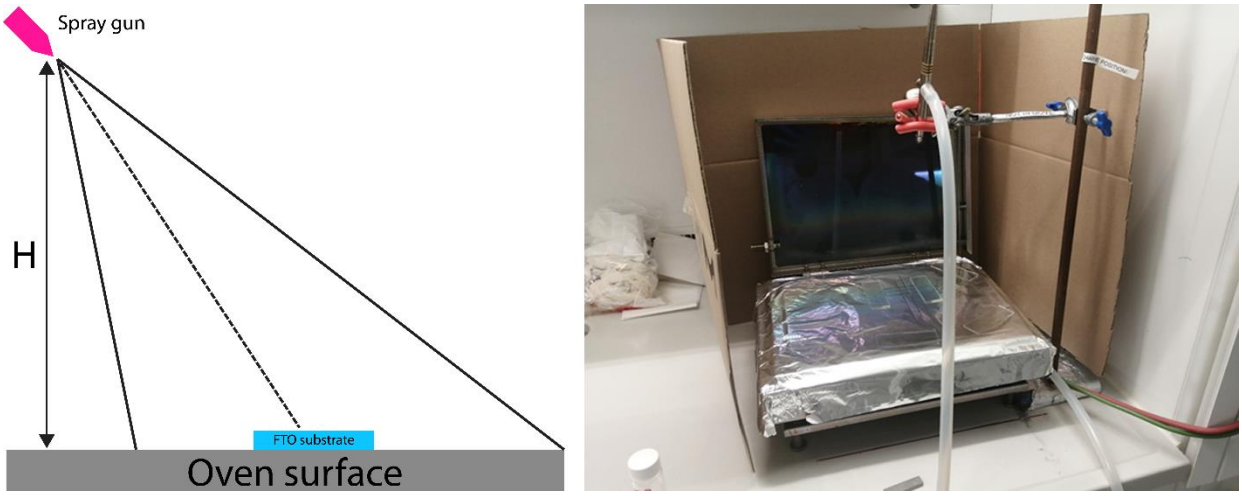

Figure 3.1. An installation diagram for spray pyrolysis.

As soon as the FTO glasses are sprayed, they are cooled down slowly to room temperature. It is possible to store the substrates with c-TiO_2 layers for several weeks (recommended maximum 4 weeks) before coating the next layer such as m-TiO_2.

3.2.4 Mesoporous TiO_2 layer

The mesoporous TiO_2 (m- TiO_2) suspension is prepared by adding 2 mL of ethanol into 0.3 g TiO_2 paste (150 mg/mL). It is recommended that the diluted paste solution is stirred overnight to ensure full dissolution. The FTO|c-TiO_2 substrate is placed in the spin coater, and 80 µl of the m-TiO_2 solution are spread on top of the substrate. The spin coating is carried out at 4000 rpm with 2000 rpm/s for 10s acceleration, followed by a drying process at 100 °C for 10 minutes. Sintering process is the next step, which is essential to calcinate FTO|c-TO_2|m-TiO_2 substrates for 30 minutes at 450 °C. As a result, a mesoporous TiO_2 layer with a thickness of 150-200 nm is obtained. The FTO|c-TO_2|m-TiO_2 substrates should be swiftly transferred into the glovebox after they are cooled down to 150 °C.

3.2.5 Perovskite layer

When working with the N_2-filled glovebox, it is important to check H_2O /O_2 levels (ideally less than 0.1 ppm), the temperature should be in the range of 24±0.5 °C, and the spin coater vacuum level as well as the programming. Hybrid perovskite films have been fabricated by utilizing different processing techniques, including solution process (mainly one-step or two step sequential deposition), vacuum deposition, and vapor assisted solution process [106]. Deposition of perovskite film via solution process is the most common method since it is straightforward to implement and low-cost. In this thesis, one-step solution deposition method has been employed for CsFAMA-based PSCs fabrication [64,107]. In general, the perovskite precursor solution was prepared comprising both organic and inorganic components, which are spin-coated on a substrate, and then the perovskite is formed with the utilize of an anti-solvent prior to the annealing treatment. The main procedure of the deposition is illustrated in Figure 3.2.

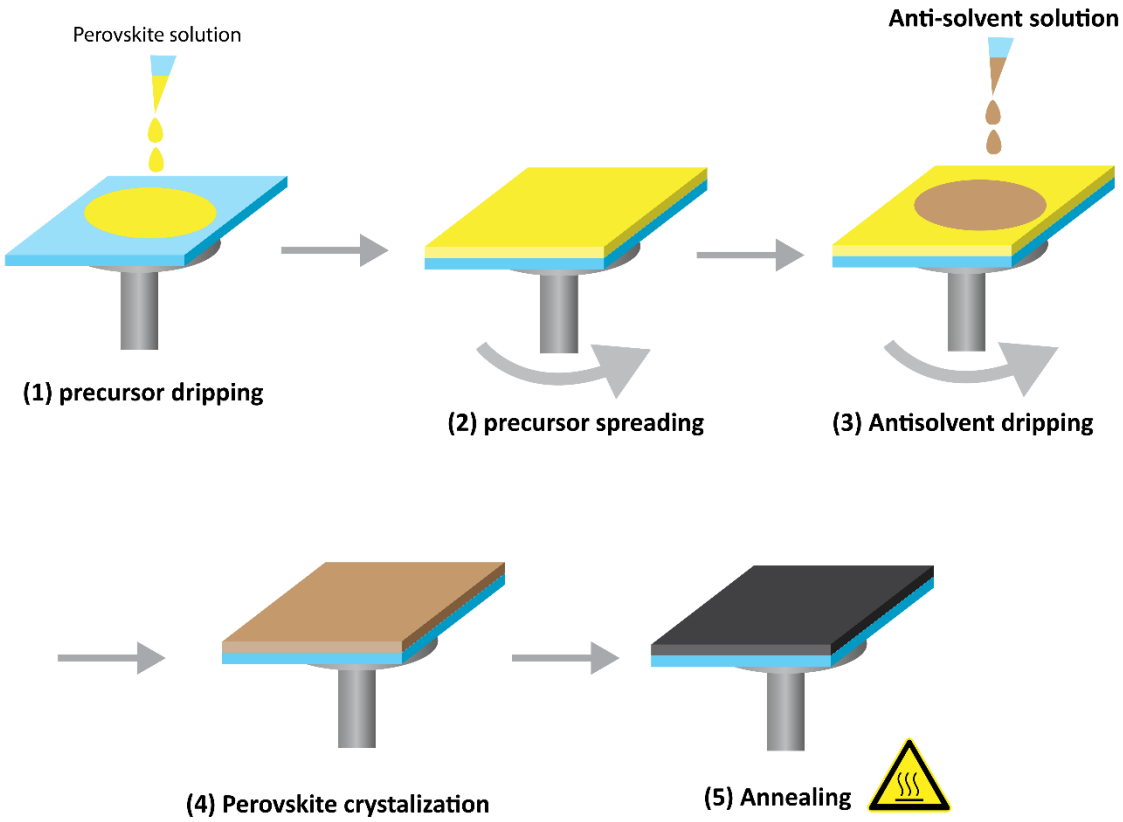

Figure 3.2. One-step perovskite deposition procedure.

First, cesium iodide (CsI) stock solution is prepared by dissolving CsI (116.91 mg) in dimethyl sulfoxide (DMSO) (300 µl), which is then heated at 60 ℃ overnight while stirring to dissolve completely. The precursor solution of CsFAMA perovskite is prepared by dissolving formamidinium iodide (147 mg), methylammonium bromide (19.2 mg), lead iodide (456.4 mg), lead bromide (66.1 mg) in 0.9 mL mixed solvent (dimethylformamide (DMF): DMSO (4:1 volume ratio)), which is kept under stirring for 30 minutes without heating. Then, CsI stock solution (36 µl) is injected into the mixture solution for continuous 48 h stirring without heating. 50 µl of perovskite solution is dropped on the FTO|c-TiO_2|m-TiO_2 substrate and then spin-coated at 1000 rpm for 10s with 200 rpm/s acceleration, immediately followed by 6000 rpm for 20s with 2000 rpm/s acceleration. The chlorobenzene anti-solvent (100 µl) is swiftly dispensed on the surface of a spinning substrate 5s before the end of the spinning. After that, the substrate is directly transferred on a hot plate at 110 ℃ for 1 hour annealing treatment. Note that the lid of the spin coater should be opened during the whole process to allow the solvent vapor to escape.

3.2.6 Hole-transport layers

The hole-transport layers used in this work are Spiro-OMeTAD as the reference, with carbazole side chain-based HTM (FL01), and TPA-based HTM (FL02). The substrates should be cooled down to room temperature before depositing the HTM layers.

The precursor solution of Spiro-OMeTAD is prepared by dissolving Spiro-OMeTAD powder (36.2 mg) in chlorobenzene (1mL), followed by heating at 60 °C for 4 minutes. At this point, the dopants, including tBP (14.4 µl), FK209 (14.4 µl), and Li-TFSI (8.8 µl), are added to the Spiro-OMeTAD solution. The Li-TFSI and FK209 stock solutions are prepared in acetonitrile with concentrations of 520 mg/ml and 300 mg/ml, respectively.

The precursor solution of FL02 HTM is prepared by dissolving TPA (10 mg) in chlorobenzene (1 mL), and by heating at 60 °C for 4 minutes. Finally, the tBP (7.2 µl), FK209 (7.2 µl), and Li-TFSI (4.4 µl) dopants are added.

The precursor solution of carbazole side chain HTM (FL01) preparation is same as that of TPA-based HTM (FL02).

The spinning programs of different HTMs are identical. Typically, 80 µl of HTM solution is swiftly dropped on the surface of FTO|c-TiO_2|m-TiO_2|CsFAMA substrate 3s after the spinning program starts (step 1: 200 rpm for 1.8 s; step 2: 1800 rpm for 30s).

After the deposition of HTM layers, the substrates are placed in a dry cabinet (<15 % RH) for overnight aging, which can enhance the oxidation of the dopants in the HTMs for a better conductivity.

3.2.7 Metal electrode contact

Finally, the electrode of gold layer (thickness of ~100 nm) is thermally evaporated under high vacuum (~ 5×10^{-6} mbar) atop the HTM layer.

3.3 Hole-only devices' fabrication

There are two types of the hole-only devices, whereas the structure (ITO|PEDOT: PSS|CsFAMA|HTM|MoO_3|Au) with the perovskite layer is for the trap density measurement and the structure without the perovskite (ITO|PEDOT: PSS|HTM|MoO_3|Au) is for the hole mobility measurement. The fabrication operation is almost the same as Mesoporous PSCs Device fabrication in term of the cleaning of FTO glasses, Perovskite and HTMs deposition, and Au evaporation. The difference is the ITO etching, PEDOT: PSS preparation, and MoO_3 evaporation.

3.3.1 ITO chemical etching and cleaning

Indium Tin Oxide (ITO) coated glass substrates (2 cm × 2 cm × 1.1 mm) are used as transparent bottom electrodes for hole-only devices. The first step is to prepare a solution of milliQ water (MQW) (30 mL), concentrated HCl (37 wt %) (27.6 mL) and concentrated nitric acid HNO_3 (65 wt %) (2.4 mL). Then, some tape is placed onto one side of of the ITO to protect part of the substrate according to a customized pattern from etching after ITO glass substrates are attached inside one Petri dish. Subsequently, an as-prepared HCl-HNO_3 solution is poured quickly into the Petri dish for immersing the glass surface for 15 minutes, the solution wets the substrates, and removes the ITO layer from the uncovered parts of the substrates. After removing the tape and ITO glass from the Petri dish, the ITO glass is cleaned with detergent and rinsed completely with distilled water, and then dried with a nitrogen gun. Finally, the resistance (expected to be more than 1 M ohm) between the etched and unetched FTO areas is checked with digital multimeter. The cleaning process of etched ITO glasses is same as the case of FTO glasses in previous Section 3.1.2.

3.3.2 PEDOT: PSS layer

First, the ITO substrate is exposed to O_3 & UV treatment for 15 minutes. PEDOT: PSS precursor solution is prepared by mixing PEDOT: PSS (1 mL) with DMF (1 mL) and the solution is well stirred for complete dissolution. The unetched ITO glass edge area is

protected by placing the tape on it. 150 µl of as-prepared PEDOT: PSS solution is extended on the ITO substrate surface which is spin-coated at 3000 rpm for 40s with 1000 rpm/s acceleration, followed by an annealing treatment on a hot plate at 150 °C for 1 hour.

3.3.3 MoO_3 and Ag layers

Finally, the perovskite on the contact side is removed by using a cotton swab and DMSO solvent. The samples are placed on the sample holder of the evaporator. MoO_3 (6 nm) and Ag (100 nm) are thermally evaporated under high vacuum (~ 6×10^{-6} mbar) atop the HTM film.

3.4 Characterization

3.4.1 *J-V* measurements

To evaluate the PCE of a solar cell, the *J-V* curve for a solar cell is recorded under one sun illumination (AM 1.5G, 100 mW/cm^2). The perovskite solar cell devices are characterized in air without encapsulation. Each cell has an aperture (20 mm^2) that defines its active area, which is accurately confirmed by an optical Dino-Lite AM4113ZTL microscope. The *J-V* characteristics are collected with a Keithley 2450 source-monitor unit. The solar simulator is AAA- solar simulator (Sciencetech Inc). The standard one-sun illumination is calibrated by using a silicon reference solar cell.

Figure 3.3 illustrates the typical set-up of the *J-V* characterization for a perovskite solar cell under one-sun condition. The solar cells are first measured in the dark and then under the illumination upon the forward and reverse scans.

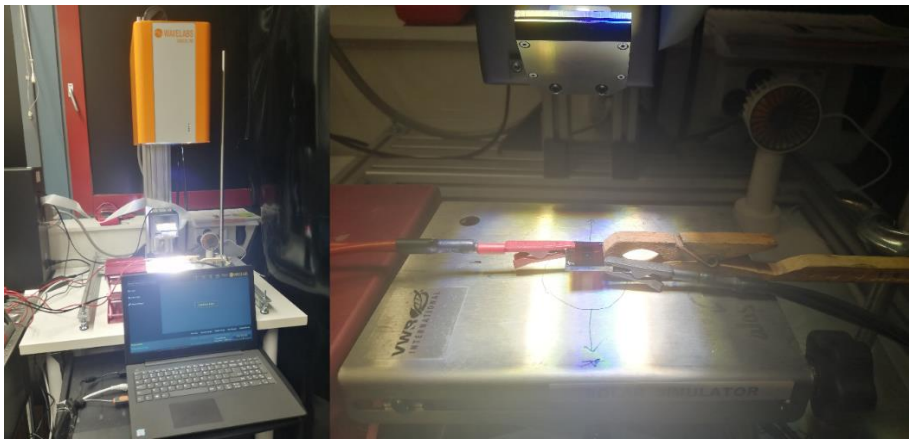

Figure 3.3 Set-up of the *J–V* characterization for one solar cell.

3.4.2 MPPT measurement

The maximum power point tracking (MPPT) is a method used for extracting maximum power from various power sources under specific conditions and the most common application used with is with photovoltaic (PV) solar systems. MPPT measurement has gained more attention for the characterization of solar cells and has become one of most reliable techniques to evaluate the PSCs stability in realistic conditions, i.e. under continuous illumination. The setup procedure is the same setup as *J-V* measurement. Also the MPPT test is performed on the unencapsulated cells with a Keithley 2450 SMU in air, under a constant illumination of LED white light (100 mW cm^{-2}) for 96 hours.

3.4.3 Hole mobility

A space-charge-limited current (SCLC) method is used for hole mobility measurement in an HTM film [108]. The typical hole-only device consists of the following structure ITO|PEDOT:PSS|HTM|MoO_3|Au [109]. In order to characterize the device, the dark current is acquired under forward bias and the hole mobility is calculated according to the following Equation (12), which is also described by Mott-Gurney [107]:

$$J = \frac{9}{8}\varepsilon_r\varepsilon_0 u\frac{v^2}{d^3} \quad (12)$$

where J is the current density, ε_r is the relative permittivity, ε_0 is the permittivity of the free space which is 8.85×10^{-14} F cm^{-1}, u is the hole mobility, d is the HTM film thickness determined by means of cross-sectional SEM image, and v is the applied bias.

3.4.4 Trap density

The trap density represents when the charge carriers in discrete levels or shallow traps happens when the quadratic dependency is just preserved, and as a result the trap density is high [110]. To measure the hole trap density, another type of hole-only device is fabricated as ITO|PEDOT: PSS|CsFAMA|HTM|MoO_3|Au [107]. The applied voltage at the common point performs the trap filled limit voltage ($\boldsymbol{V_{TFL}}$) [111], that is used to evaluate the trap density $\boldsymbol{n_{trap}}$ by using the following Equation (13):

$$\boldsymbol{n_{trap} = \frac{2\varepsilon_r \varepsilon_0 V_{TFL}}{eL^2}} \quad \textbf{(13)}$$

where e is the elementary charge and L is the thickness of the perovskite layer.

3.4.5 Photoluminescence (PL) spectra

PL refers to the phenomenon in which photons, or light energy, induce an emission of a photon from any substance. It is contactless and nondestructive probing materials technique. The materials used in PL are fluorescence and phosphorescence. PL is widely used to characterize the semiconductor properties to determine the direct bandgap of semiconductors or HOMO-LUMO gap in molecules by means of the emitted photon energy, which is direct measure the difference of energy between the involved bonds [112]. In this work, the Pico Quant Fluotime 300 is used to measure the steady-state PL spectra using a 600 nm excitation light. The quenching efficiency, also known as the hole injection yield, may be evaluated by comparing the PL spectra amplitude of pure perovskite films before and after HTM deposition.

4 RESULTS AND DISCUSSION

The hole trap density of CsFAMA-based *n-i-p* standard devices and the hole transporting properties with different HTMs including Spiro-OMeTAD, FL01, and FL02 have been investigated. Moreover, the photoluminescence (PL) quenching measurements have been performed to investigate the process of the hole extraction at the perovskite/HTM interface. Finally, the performance and stability of the devices have been also studied.

4.1 Hole transporting property and trap density

To clarify the hole transporting properties in relation to the different HTM molecular structures, the hole mobilities were measured by using conducting SCLC method, on samples doped with FL01, and FL02, and Spiro-OMeTAD as reference. Figure 4.1 illustrates the comparison of dark $J-V^2$ curves of the hole-only devices with structure "ITO|PEDOT:PSS|HTM|MoO_3|Au". Their hole mobilities were extracted based on formula (12)

$$\boldsymbol{J = \frac{9}{8}\varepsilon_r\varepsilon_0 u\frac{v^2}{d^3}} \qquad \textbf{(12)}$$

The mobility values are summarized in Table 2. FL02 HTM exhibits a much higher hole mobility (5.3×10^{-4} cm^2 V^{-1} s^{-1}) than FL01 HTM (9.8×10^{-5} cm^2 V^{-1} s^{-1}). This suggests that the twisted side chain of FL02 molecule is rather beneficial for the intermolecular charge transport compared to the linear side chain of FL01. Moreover, the hole mobility of doped FL02 HTM is in the same order of that of doped Spiro-OMeTAD HTM, possibly suggesting that the charge transfer within the FL02 HTM could be efficient from the device point of view.

Furthermore, to assess the hole trap density related to the surface passivation, another type of hole-only devices with structure "ITO|PEDOT:PSS|CsFAMA|HTM|MoO_3|Au" was fabricated. The dark $J-V$ curves of Spiro-OMeTAD, FL01, and FL02-based hole-only

devices are illustrated in Figure 4.2. The applied voltage at the kink point performs the trap-filled limit voltage (V_{TFL}), that allows to calculate the trap density $\boldsymbol{n_{trap}}$ from equation (13)

$$\boldsymbol{n_{trap}} = \frac{2\varepsilon_r\varepsilon_0 V_{TFL}}{eL^2} \qquad \textbf{(13)}$$

The calculated $\boldsymbol{n_{trap}}$ values are summarized in Table 2. The FL02-based device shows a lower trap density than that of FL01-based one, mainly attributed to the reduced surface defects of the perovskite upon the passivation of twisted side chain of FL02 that functionalizes the perovskite surface. The higher hole mobility and lower trap density of FL02 HTM potentially predict a better performance of their corresponding devices compared to FL01 HTM.

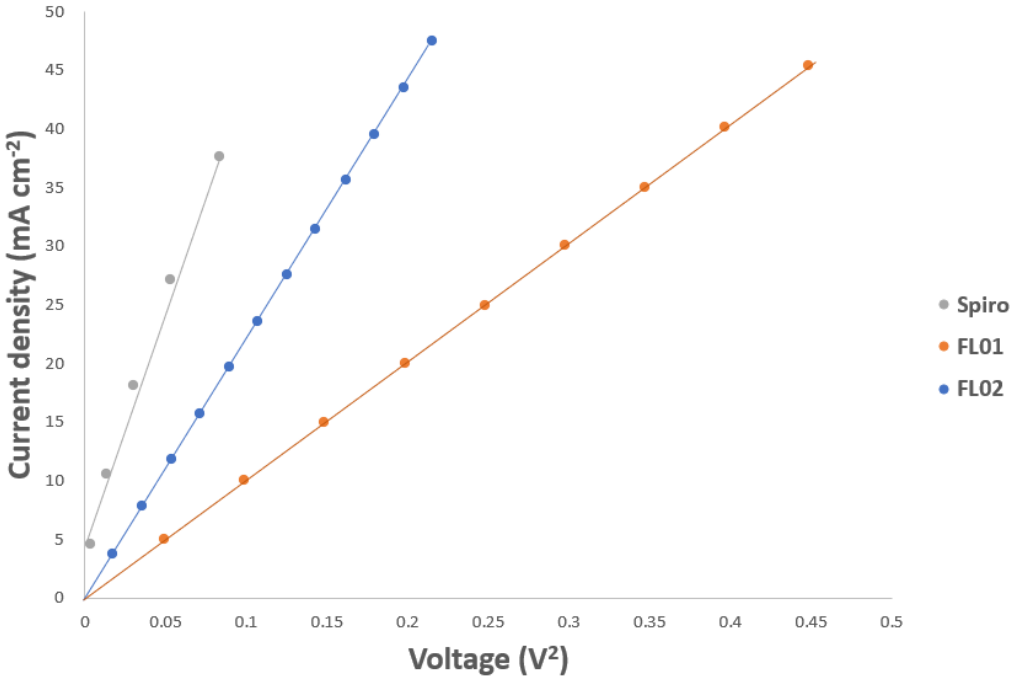

Figure 4.1. Dark current density-voltage (J-V^2) curves for hole-only devices with structure "ITO|PEDOT: PSS|HTM|MoO_3|Au". Solid lines show the fitting results with a linear function (Equation 12).

Table 2. Hole transporting Mobility (μ_h), trap density (n_{trap}), and PL quenching efficiency of Spiro-OMeTAD, FL01, and FL02

HTM	μ_h (cm^2 V^{-1} s^{-1})	n_{trap} (cm^{-3})	PL Quenching efficiency (%)
Spiro-OMeTAD	7.5×10^{-4}	4.48×10^{15}	98.2 %
FL01	9.8×10^{-5}	6.95×10^{15}	77.0 %
FL02	5.3×10^{-4}	5.56×10^{15}	95.8 %

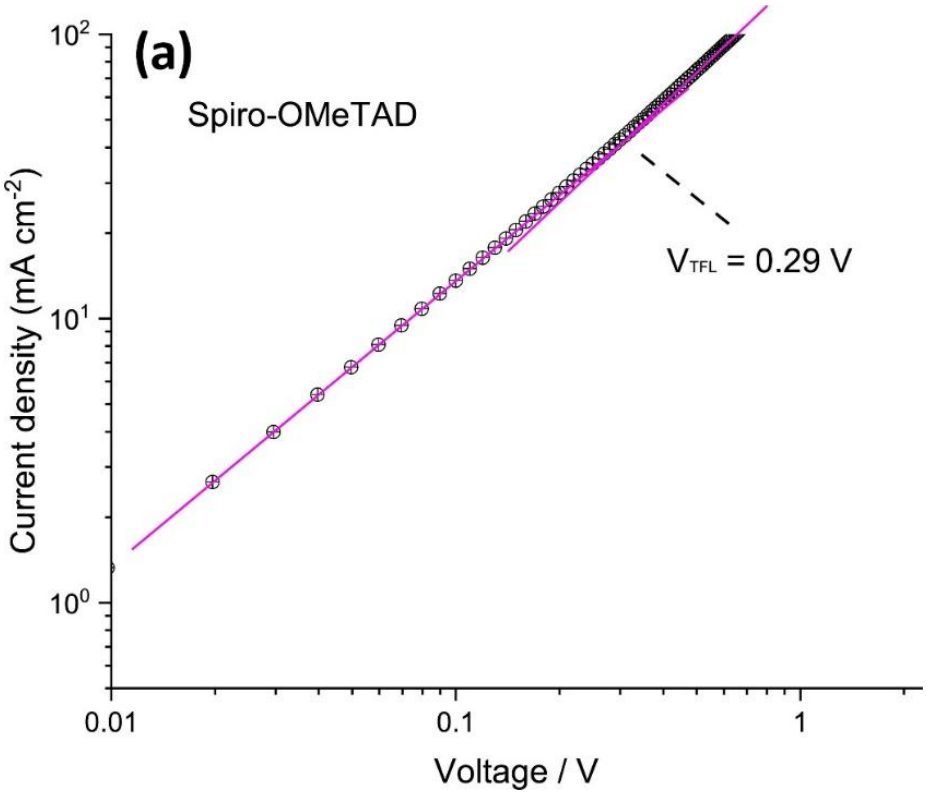

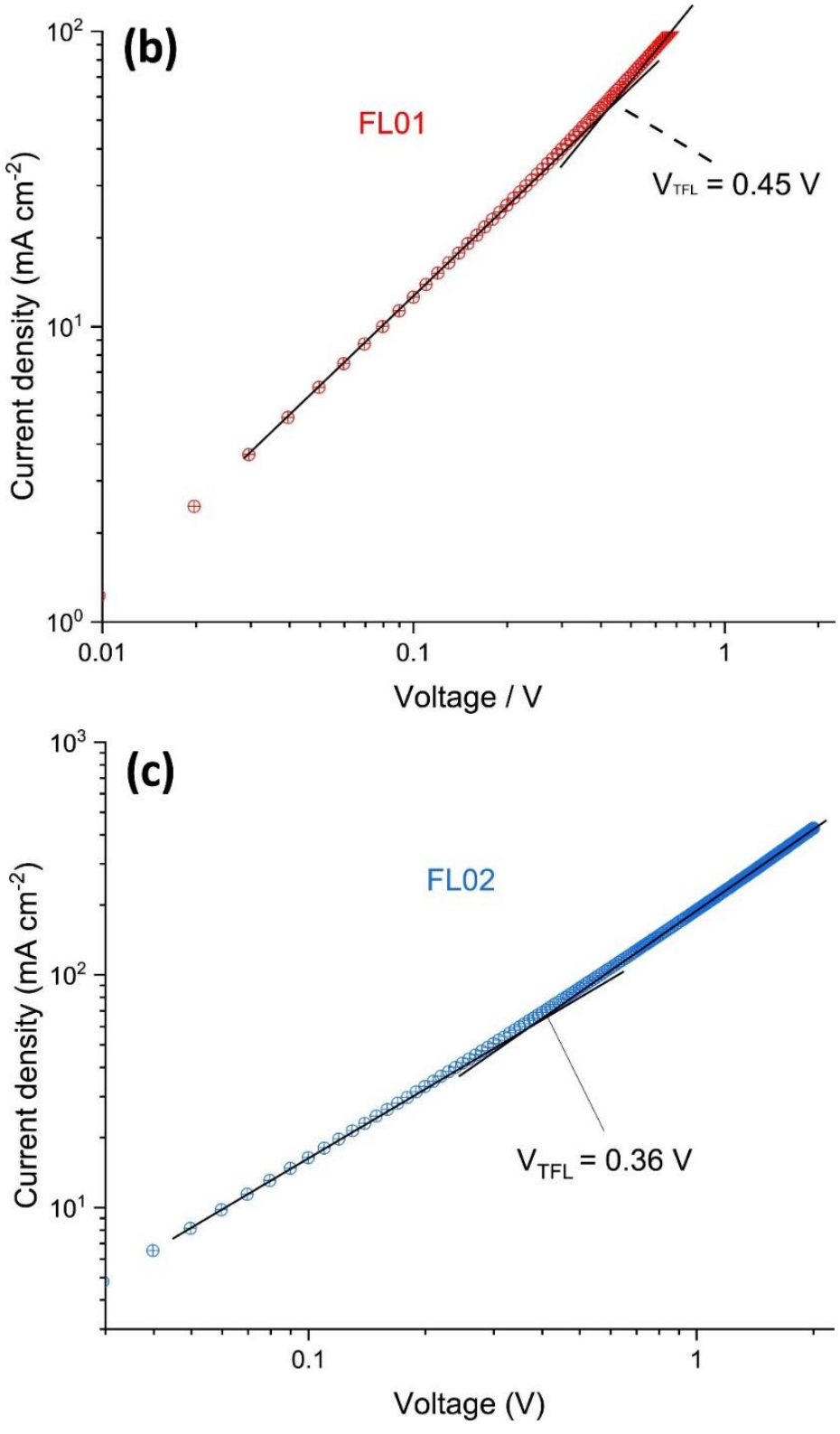

Figure 4.2 Dark *J–V* curves of hole-only devices with structure 'ITO/PEDOT: PSS/perovskite/HTM/MoO_3/Au' with V_{TFL} kink point extraction.

4.2 Photoluminescence (PL) quenching measurements

The PL quenching experiments were conducted by recording the PL spectra of the glass|CsFAMA sample coated with and without the HTMs, as shown in Figure 4.3. By comparing with the integrated PL intensity of pure CsFAMA perovskite sample, the PL quenching efficiencies can be calculated, as summarized in Table 2. The glass|CsFAMA|FL02 sample demonstrates much higher quenching efficiency (95.8 %) compared to that (77.0 %) of FL01 case, indicating that the holes can be efficiently extracted from the valence band of perovskite to the HOMO level of FL02, thanks to the close attachment of the twisted side chain of FL02 on the perovskite surface. It is also noted that the glass|CsFAMA|Spiro-OMeTAD sample shows even higher quenching efficiency (98.2 %) than the corresponding sample with FL02. This is consistent with the higher short-circuit current (J_{sc}) obtained for the reference Spiro-OMeTAD-based devices, as will be discussed in detail later.

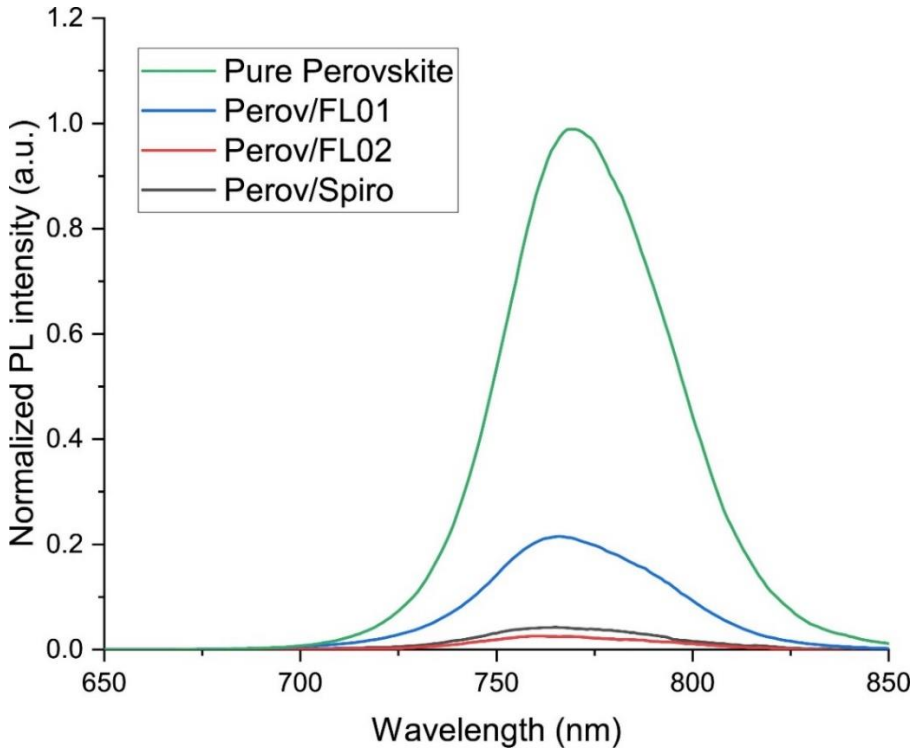

Figure 4.3. PL spectra of the perovskite films coated with and without HTMs using 600 nm excitation light.

The PL quenching efficiency (as in Table 2) is 77.0 %, 95.8 %, and 98.2 % for FL01, FL02, and Spiro-OMeTAD, respectively.

4.3 Performance of FL01 and FL02 HTMs-based *n-i-p* devices

Figure 4.4 illustrates the trend of the photovoltaic (PV) parameters PCE, FF, Voc and Jsc of the champion devices employing the different HTMs, i.e., Spiro-OMeTAD, FL01, and FL02. Surprisingly, FL02-based devices exhibit more than double PCE (maximum of 17.8 %) compared to that (8.6 %) of FL01-based ones, ascribed to the significant enhancement in all the PV parameters. We attribute the performance boost to the enlarged hole mobility of FL02 HTM molecules as well as the improved interfacial hole extraction dynamics at the interface between perovskite and FL02 HTM. Both factors (hole mobility and hole extraction interfacial dynamics) benefit from a higher twisting level in the side chain of FL02 compared with FL01. Interestingly, when comparing the FL02 device performance with that of the reference (based on Spiro-OMeTAD), the loss of PCE is only around 1 %. Indeed, FL02-based devices even show higher FF than that of Spiro-OMeTAD-based ones, indicating that the surface defects of CsFAMA perovskite could be more effectively reduced upon the passivation from the attachment of the twisted side chain of FL02 on the perovskite surface. **Table 3** summarizes the performance (best and average values) of as-fabricated PSCs with different HTMs, based on 15 cells in each case. Figure 4.5 shows the comparison of the $J-V$ curves (forward and reverse scans) of the champion devices, measured under one-sun illumination (AM 1.5G, 100 mW/cm^2). It is noted that the hysteresis (H-index = 1.12) of FL02-based devices is reduced compared to that (H-index = 1.24) of FL01-based ones, further suggesting that the functionalization of the twisted side chain of FL02 on the perovskite surface is indeed favorable for the defect passivation by decreasing the ion migration at the interface.

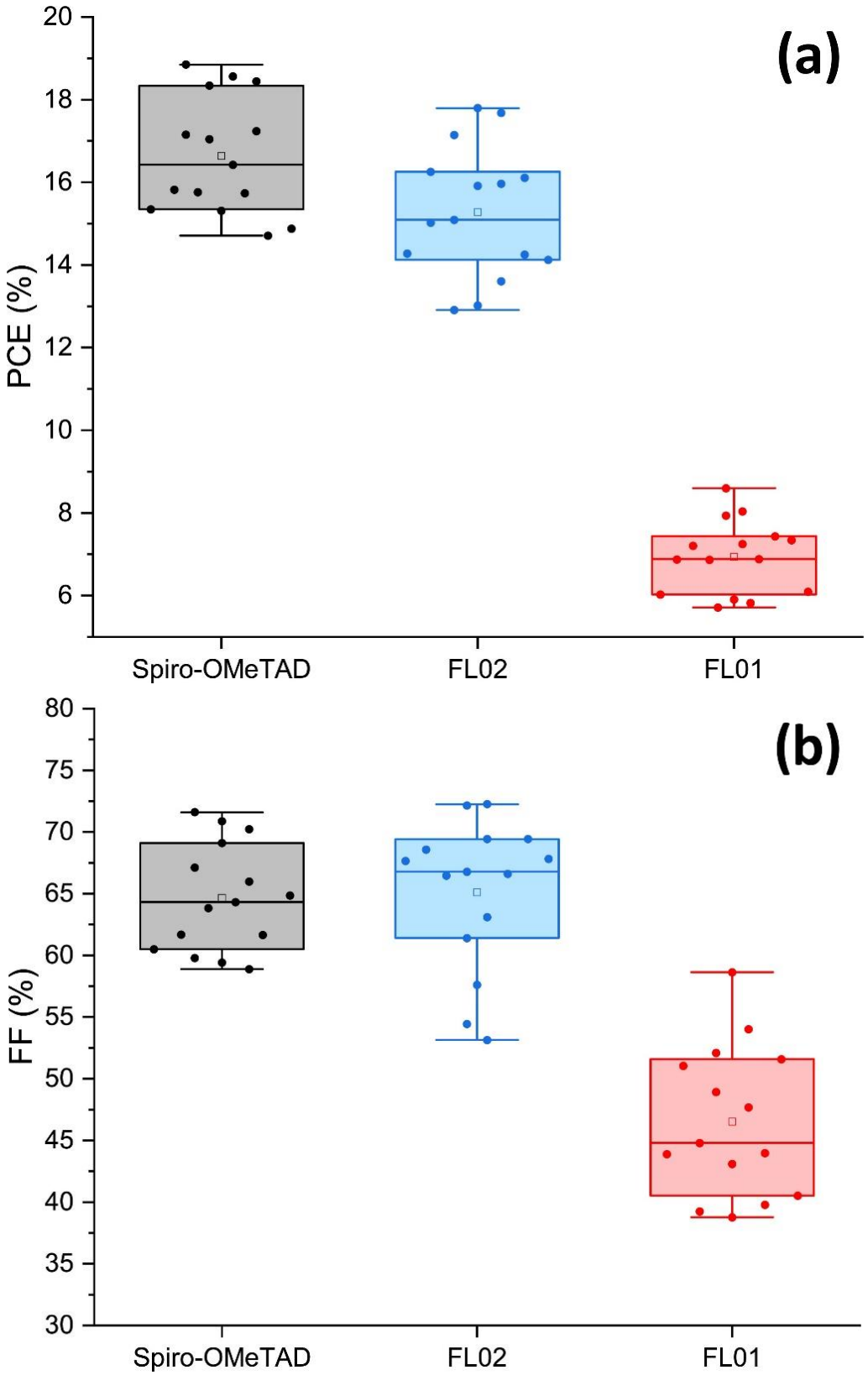
(a)
PCE (%)
20
18
16
14
12
10
8
6
Spiro-OMeTAD
FL02
FL01
(b)
FF (%)
80
75
70
65
60
55
50
45
40
35
30
Spiro-OMeTAD
FL02
FL01

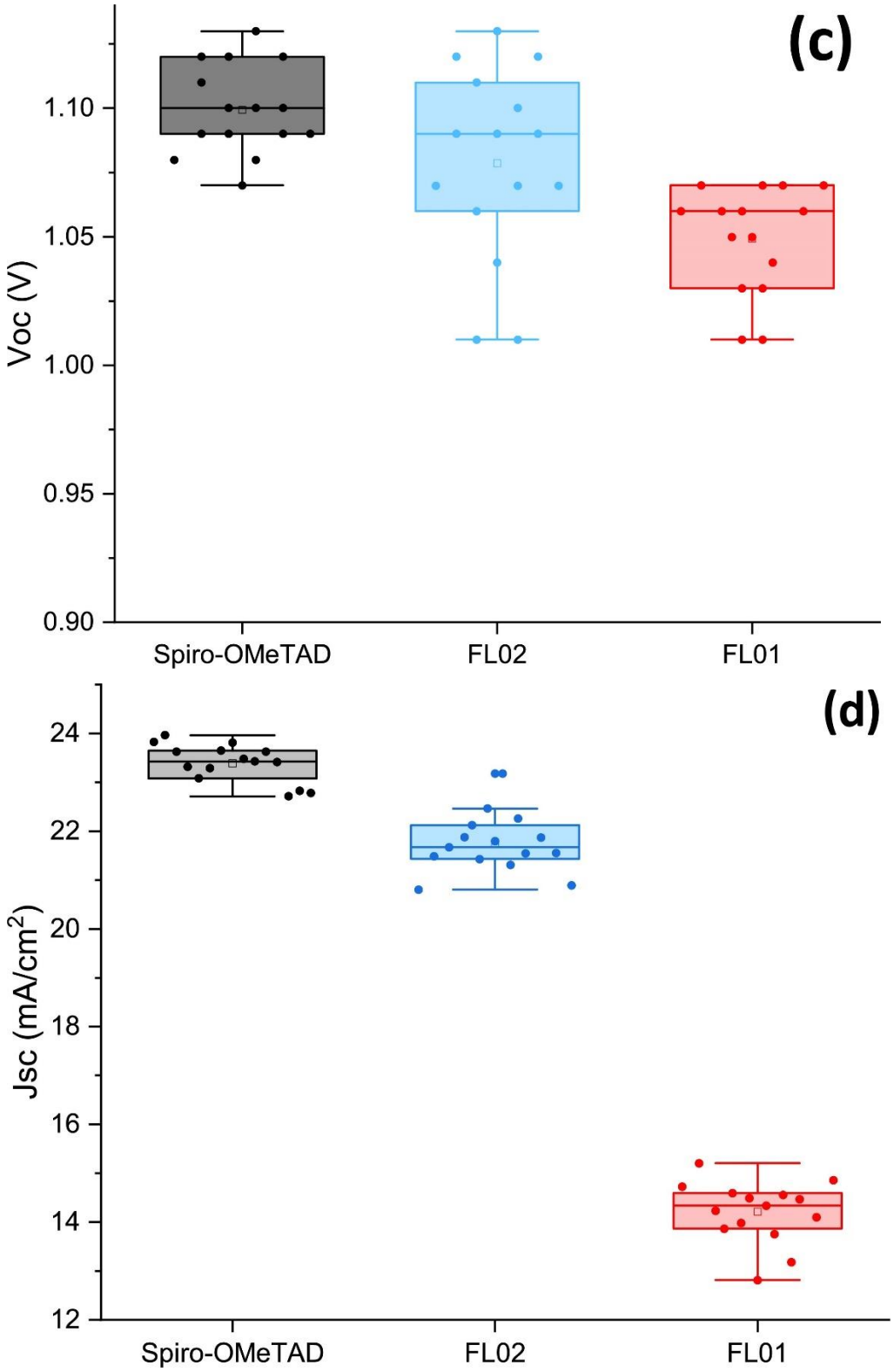

Figure 4.4. PV parameters (a) PCE, (b) FF, (c) V_{oc}, and (d) J_{sc}, derived from the *J*–*V* scans recorded for 15 different cells.

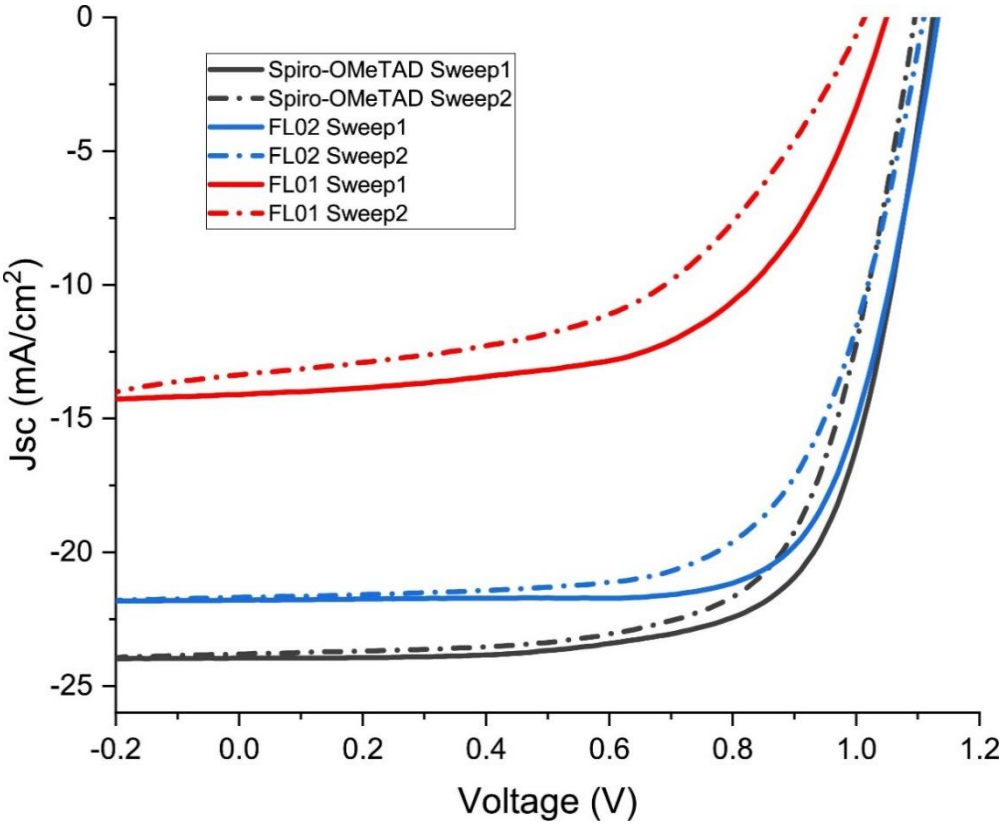

Figure 4.5. $J-V$ curves of the best devices with FL01, FL02, and Spiro-OMeTAD under one-sun illumination with reverse (Sweep 1) and forward (Sweep 2) scans. The scan rate is 20 mV/s.

Table 3. PV parameters, PCE, FF, V_{oc}, and J_{sc}, derived from the J–V scans recorded for 15 cells. All PV parameters data are acquired from the reverse scan.

Sample	**PCE (%)**		**FF (%)**		**J_{sc} (mA/cm2)**		**V_{oc} (V)**		**H-Index**	
	Best	**Avg.**	**Best**	**Avg.**	**Best**	**Avg.**	**Best**	**Avg.**	**Best**	**Avg.**
Spiro-OMeTAD	18.8	16.6	70.2	64.7	24.0	23.4	1.1	1.1	1.07	1.05
FL01	8.6	6.9	58.6	46.5	14.1	14.2	1.0	1.0	1.24	1.26
FL02	17.8	15.3	72.2	65.1	21.8	21.8	1.1	1.1	1.12	1.15

4.4 Stability Study

To investigate the degradation processes taking place in the devices, the stabilities of unencapsulated PSCs with different HTMs have been recorded by analyzing the evolution of different PV parameters (Figure 4.6) of the champion devices as a function of storage time. The samples were measured under ambient conditions (RH ~ 40 %) and stored in dry conditions (in darkness, RH < 10 %).

In Figure 4.6 (a), the FL02-based devices exhibit an impressive stability compared to either reference Spiro-OMeTAD- or FL01-based counterparts. The PCE of FL02-based PSC shows no obvious drop after reaching the peak value upon the first 5 days storage, while the PCE of FL01-based device decreases to around 60 % of its initial value after over 70 days storage, which is similar to the degradation trend of Spiro-OMeTAD reference cell. Both FF and V_{oc} gradually increase during the long-term storage in the case of FL02 HTM, mainly contributing to its high long-term stability. This, in turn, indicates that the passivation promoted by the twisted side chain of FL02 can not only improve the interfacial charge transfer but also reduce the surface defects (e.g., traps and pin-holes) of the perovskite, which can effectively prevent the penetration of moisture and oxygen into the perovskite layer.

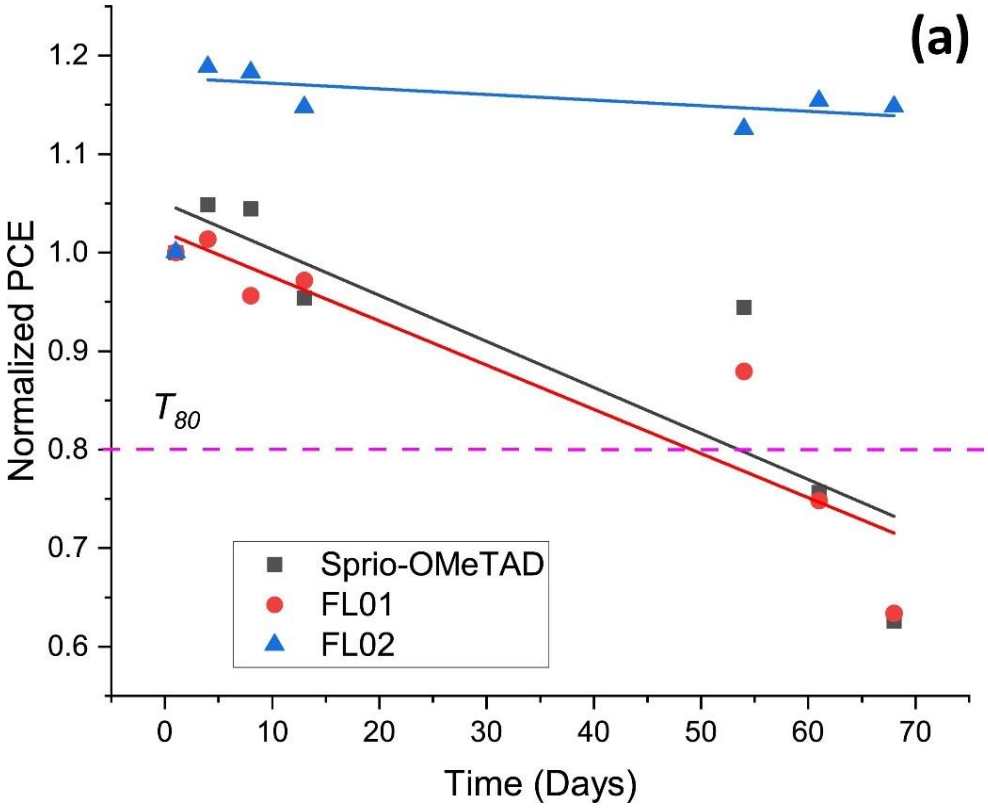
(a)
Normalized PCE
Time (Days)
T_{80}
Sprio-OMeTAD
FL01
FL02

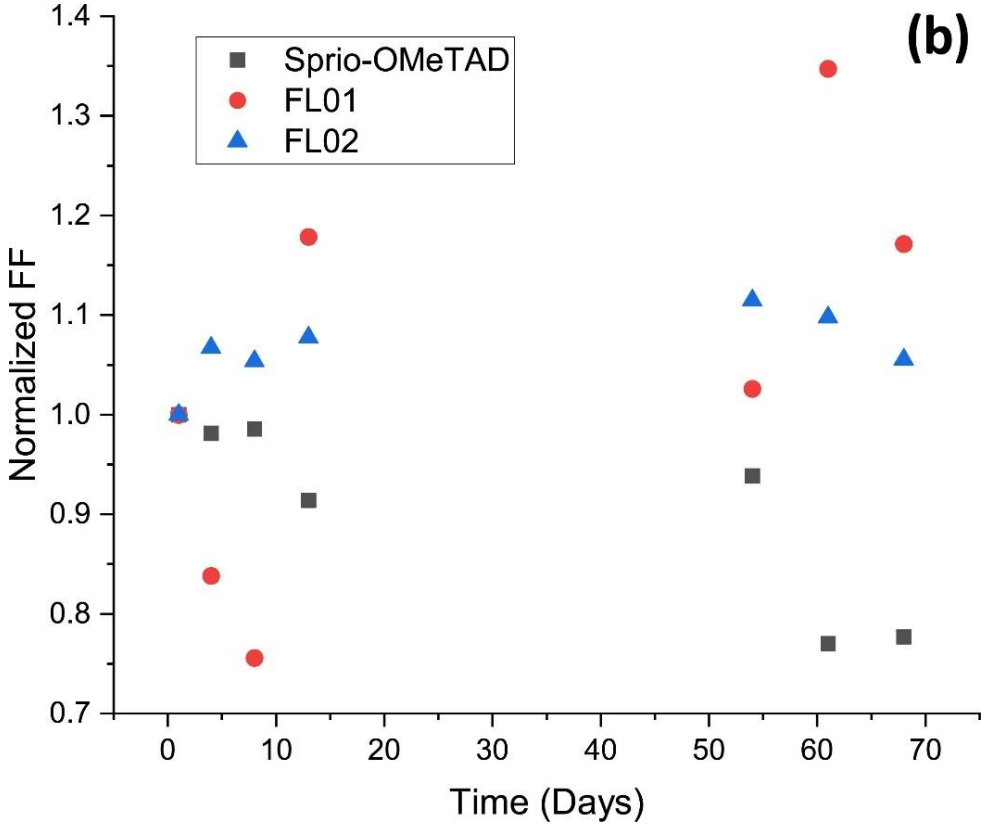
(b)
Normalized FF
Time (Days)
Sprio-OMeTAD
FL01
FL02

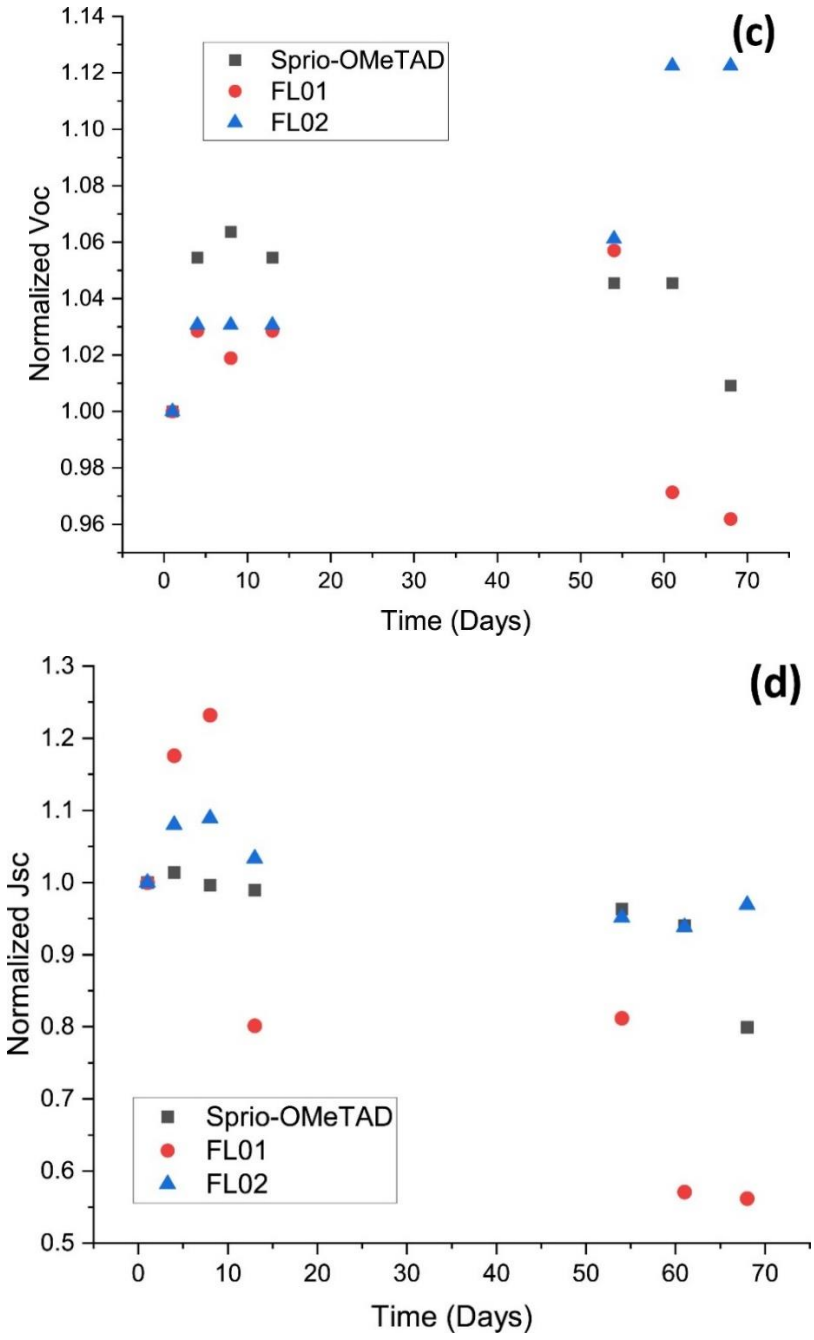

Figure 4.6. Normalized PV parameters (a) PCE, (b) FF, (c) V_{oc}, and (d) J_{sc} of the PSCs with different HTMs vs. storage time, measured in ambient conditions (RH ~ 40 %) and stored in dry air (in darkness, RH < 10 %). T_{80} is the time at which PCE parameter drops to 80 % of its initial value. The linear fit in (a) shows stability trend to derive the T_{80} shelf-life (53 and 49 days, respectively) of Spiro-OMeTAD and FL01 devices.

To further confirm the photostability of the devices, the MPPT tests were conducted for the unencapsulated champion devices under the continuous one-sun illumination, as shown in Figure 4.7. The FL02-based device shows the highest stability with a T_{80} lifetime of >98 h while that of FL01-based one is limited to 32 h. This trend is consistent with above mentioned shelf-lifetimes.

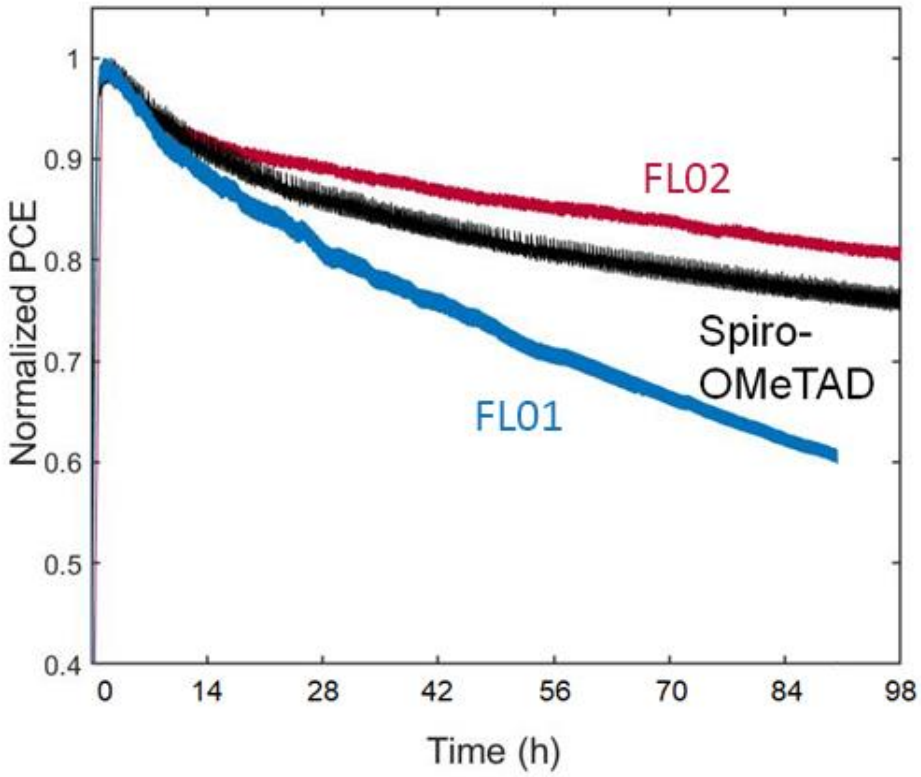

Figure 4.7. MPPT tests of the unencapsulated PSCs with different HTMs under continuous 1-sun illumination (100 mW cm^{-2}).

5 CONCLUSIONS

In this work, the performance and the stability of standard *n-i-p* mesoscopic PSC devices, with a triple-cation CsFAMA perovskite light-harvesting layer, employing a novel organic HTM, namely FL02, in alternative to the widely used yet expensive Spiro-OMeTAD, were systematically investigated. The cost-effective FL02 HTM features good hole transport properties due to the twisted side chain in the molecular design, as evident from the comparison with a reference HTM (FL01) containing a planar side chain.

According to the experimental characterization of PSCs with different HTMs, FL02-based devices exhibit high PCEs (17.8 % for the champion device) compared to that (8.6 %) of FL01-based devices, due to the high hole extraction efficiency and low trap density at the perovskite/HTM interface. This result is based on the strong passivation effect of the twisted side chain of FL02 on the perovskite surface. It is noted that the PCE loss is only around 1 % when comparing the performance of FL02-based devices with that of commercially available Spiro-OMeTAD-based ones, suggesting that the newly designed FL02 has good potential to replace the traditional Spiro-OMeTAD. Moreover, the hysteresis of the FL02-based devices is reduced compared to that of FL01-based ones, hinting that FL02 is more favorable for the surface passivation by decreasing the ion migration at the perovskite/HTM interface. Importantly, the FL02-based devices exhibit an impressive stability by showing no obvious drop in PCE after over 70 days of storage in dry air, while the PCE of FL01-based devices decrease to around 60 % of its initial value during the same period. This is also similar to the degradation trend of Spiro-OMeTAD reference cells, due to the effective protection of the perovskite surface by the functionalization of the twisted side chain of FL02 at the interface.

We conclude that FL02 can enhance the interfacial charge transfer as well as reduce the surface defects of the perovskite, avoiding the penetration of moisture and oxygen into the perovskite layer. This has been in turn evidenced by the long T_{80} lifetime of >98 h of unencapsulated FL02-based devices under continuous one-sun illumination (MPPT test), which is longer than the commonly reported T_{80} lifetime (<50 h) under identical test conditions. However, the T_{80} lifetime of FL01 cells is limited to 32 h.

The side chain engineering of small molecular HTMs is a promising strategy to functionalize the perovskite surface in *n-i-p* device structures. This work provides molecular design guidelines for novel organic HTMs enabling the development of low-cost, efficient, and stable PSCs.

REFERENCES

[1] G. Lozano, M. Anaya, M.E. Calvo, H. Mi´guez, Optical design of all-perovskite tandem solar cells, in: Optics InfoBase Conference Papers, 2017. https://doi.org/10.1364/PV.2017.PTu1A.3.

[2] J. Cui, H. Yuan, J. Li, X. Xu, Y. Shen, H. Lin, M. Wang, Recent progress in efficient hybrid lead halide perovskite solar cells, Sci Technol Adv Mater. 16 (2015). https://doi.org/10.1088/1468-6996/16/3/036004.

[3] Y. Cai, L. Liang, P. Gao, Promise of commercialization: Carbon materials for low-cost perovskite solar cells, Chinese Physics B. 27 (2018). https://doi.org/10.1088/1674-1056/27/1/018805.

[4] R. Perez, M. Perez, A Fundamental Look At Energy Reserves For The Planet, The International Energy Agency SHC Programme Solar Update. 50 (2009).

[5] Q. Xu, D. Yang, J. Lv, Y.Y. Sun, L. Zhang, Perovskite Solar Absorbers: Materials by Design, Small Methods. 2 (2018). https://doi.org/10.1002/smtd.201700316.

[6] M.A. Green, K. Emery, Y. Hishikawa, W. Warta, E.D. Dunlop, Solar cell efficiency tables (version 41), Progress in Photovoltaics: Research and Applications. 21 (2013). https://doi.org/10.1002/pip.2352.

[7] S. Mathew, A. Yella, P. Gao, R. Humphry-Baker, B.F.E. Curchod, N. Ashari-Astani, I. Tavernelli, U. Rothlisberger, M.K. Nazeeruddin, M. Grätzel, Dye-sensitized solar cells with 13% efficiency achieved through the molecular engineering of porphyrin sensitizers, Nat Chem. 6 (2014). https://doi.org/10.1038/nchem.1861.

[8] M. Aamir Iqbal, M. Malik, W. Shahid, S. Zaheer Ud Din, N. Anwar, M. Ikram, F. Idrees, Materials for Photovoltaics: Overview, Generations, Recent Advancements and Future Prospects, in: Thin Films Photovoltaics, 2022. https://doi.org/10.5772/intechopen.101449.

[9] T. Ibn-Mohammed, S.C.L. Koh, I.M. Reaney, A. Acquaye, G. Schileo, K.B. Mustapha, R. Greenough, Perovskite solar cells: An integrated hybrid lifecycle assessment and review in comparison with other photovoltaic technologies, Renewable and Sustainable Energy Reviews. 80 (2017). https://doi.org/10.1016/j.rser.2017.05.095.

[10] A. Kojima, K. Teshima, Y. Shirai, T. Miyasaka, Organometal halide perovskites as visible-light sensitizers for photovoltaic cells, J Am Chem Soc. 131 (2009). https://doi.org/10.1021/ja809598r.

[11] P. Zhang, M. Li, W.C. Chen, A Perspective on Perovskite Solar Cells: Emergence, Progress, and Commercialization, Front Chem. 10 (2022). https://doi.org/10.3389/fchem.2022.802890.

[12] A. Chilvery, S. Das, P. Guggilla, C. Brantley, A. Sunda-Meya, A perspective on the recent progress in solution-processed methods for highly efficient perovskite solar cells, Sci Technol Adv Mater. 17 (2016) 650–658. https://doi.org/10.1080/14686996.2016.1226120.

[13] D. Zhou, T. Zhou, Y. Tian, X. Zhu, Y. Tu, Perovskite-Based Solar Cells: Materials, Methods, and Future Perspectives, J Nanomater. 2018 (2018). https://doi.org/10.1155/2018/8148072.

[14] S. Ameen, M.A. Rub, S.A. Kosa, K.A. Alamry, M.S. Akhtar, H.S. Shin, H.K. Seo, A.M. Asiri, M.K. Nazeeruddin, Perovskite Solar Cells: Influence of Hole Transporting Materials on Power Conversion Efficiency, ChemSusChem. 9 (2016). https://doi.org/10.1002/cssc.201501228.
[15] E. Raza, F. Aziz, Z. Ahmad, Stability of organometal halide perovskite solar cells and role of HTMs: recent developments and future directions, (2018). https://doi.org/10.1039/c8ra03477j.
[16] J. Urieta-Mora, I. García-Benito, A. Molina-Ontoria, N. Martín, Hole transporting materials for perovskite solar cells: a chemical approach, Chem Soc Rev. 47 (2018). https://doi.org/10.1039/c8cs00262b.
[17] E. Kasparavicius, M. Franckevič, V. Malinauskiene, K. Genevič, V. Getautis, T. Malinauskas, Oxidized Spiro-OMeTAD: Investigation of Stability in Contact with Various Perovskite Compositions, (2021). https://doi.org/10.1021/acsaem.1c02375.
[18] W.J. Yin, T. Shi, Y. Yan, Unique properties of halide perovskites as possible origins of the superior solar cell performance, Advanced Materials. 26 (2014). https://doi.org/10.1002/adma.201306281.
[19] S. Moghadamzadeh, Multi-cation perovskite semiconductors for all-perovskite tandem solar cells, (2021). https://doi.org/10.5445/IR/1000130564.
[20] A.K. Jena, A. Kulkarni, T. Miyasaka, Halide Perovskite Photovoltaics: Background, Status, and Future Prospects, Chem Rev. 119 (2019) 3036–3103. https://doi.org/10.1021/acs.chemrev.8b00539.
[21] T. Duc Duong, Development of High Efficiency Four-Terminal Perovskite-Silicon Tandems, 2017.
[22] H.S. Jung, N.G. Park, Perovskite solar cells: From materials to devices, Small. 11 (2015) 10–25. https://doi.org/10.1002/smll.201402767.
[23] R. Fu, W. Zhou, Q. Li, Y. Zhao, D. Yu, Q. Zhao, Stability Challenges for Perovskite Solar Cells, ChemNanoMat. 5 (2019) 253–265. https://doi.org/10.1002/cnma.201800503.
[24] Z. Xiao, Z. Song, Y. Yan, From Lead Halide Perovskites to Lead-Free Metal Halide Perovskites and Perovskite Derivatives, Advanced Materials. 31 (2019). https://doi.org/10.1002/adma.201803792.
[25] J. Huang, Z. Yin, Q. Zheng, Applications of ZnO in organic and hybrid solar cells, Energy Environ Sci. 4 (2011). https://doi.org/10.1039/c1ee01873f.
[26] D.Y. Son, J.W. Lee, Y.J. Choi, I.H. Jang, S. Lee, P.J. Yoo, H. Shin, N. Ahn, M. Choi, D. Kim, N.G. Park, Self-formed grain boundary healing layer for highly efficient CH3 NH3 PbI3 perovskite solar cells, Nat Energy. 1 (2016). https://doi.org/10.1038/nenergy.2016.81.
[27] Y. Wang, Y. Liang, Y. Zhang, W. Yang, L. Sun, D. Xu, Y. Wang, Y. Liang, Y. Zhang, L. Sun, W. Yang, D. Xu, FULL PAPER www.afm-journal.de Pushing the Envelope: Achieving an Open-Circuit Voltage of 1.18 V for Unalloyed MAPbI 3 Perovskite Solar Cells of a Planar Architecture, (2018). https://doi.org/10.1002/adfm.201801237.
[28] M. Jung, T.J. Shin, J. Seo, G. Kim, S. il Seok, Structural features and their functions in surfactant-armoured methylammonium lead iodide perovskites for highly efficient and stable solar cells †, 2188 | Energy Environ. Sci. 11 (2018) 2188. https://doi.org/10.1039/c8ee00995c.

[29] B. Conings, J. Drijkoningen, N. Gauquelin, A. Babayigit, A. Ethirajan, J. Verbeeck, J. Manca, E. Mosconi, F. de Angelis, H.-G. Boyen, B. Conings, J. Drijkoningen, A. Babayigit, A. Ethirajan, H. Boyen, N. Gauquelin, J. Verbeeck, E. Mosconi, F. de Angelis, Intrinsic Thermal Instability of Methylammonium Lead Trihalide Perovskite, (2015). https://doi.org/10.1002/aenm.201500477.

[30] Y. Han, S. Meyer, Y. Dkhissi, K. Weber, J.M. Pringle, U. Bach, L. Spiccia, Y.-B. Cheng, Degradation observations of encapsulated planar CH 3 NH 3 PbI 3 perovskite solar cells at high temperatures and humidity, (2015). https://doi.org/10.1039/c5ta00358j.

[31] N. Aristidou, I. Sanchez-Molina, T. Chotchuangchutchaval, M. Brown, L. Martinez, T. Rath, S.A. Haque, The Role of Oxygen in the Degradation of Methylammonium Lead Trihalide Perovskite Photoactive Layers, Angewandte Chemie - International Edition. 54 (2015). https://doi.org/10.1002/anie.201503153.

[32] Q. Wang, N. Phung, D. di Girolamo, P. Vivo, A. Abate, Enhancement in lifespan of halide perovskite solar cells, Energy Environ Sci. 12 (2019) 865–886. https://doi.org/10.1039/c8ee02852d.

[33] L. Krückemeier, U. Rau, M. Stolterfoht, T. Kirchartz, How to Report Record Open-Circuit Voltages in Lead-Halide Perovskite Solar Cells, (2019). https://doi.org/10.1002/aenm.201902573.

[34] Y. Zhang, S. Seo, ⊥ Soo, Y. Lim, Y. Kim, S.-G. Kim, D.-K. Lee, S.-H. Lee, H. Shin, H. Cheong, N.-G. Park, Achieving Reproducible and High-Efficiency (>21%) Perovskite Solar Cells with a Presynthesized FAPbI 3 Powder, 13 (2019) 39. https://doi.org/10.1021/acsenergylett.9b02348.

[35] S. Xu, A. Libanori, G. Luo, J. Chen, Engineering bandgap of CsPbI3 over 1.7 eV with enhanced stability and transport properties, IScience. 24 (2021). https://doi.org/10.1016/j.isci.2021.102235.

[36] N. Pellet, P. Gao, G. Gregori, T.Y. Yang, M.K. Nazeeruddin, J. Maier, M. Grätzel, Mixed-organic-cation perovskite photovoltaics for enhanced solar-light harvesting, Angewandte Chemie - International Edition. 53 (2014). https://doi.org/10.1002/anie.201309361.

[37] D.P. McMeekin, G. Sadoughi, W. Rehman, G.E. Eperon, M. Saliba, M.T. Hörantner, A. Haghighirad, N. Sakai, L. Korte, B. Rech, M.B. Johnston, L.M. Herz, H.J. Snaith, A mixed-cation lead mixed-halide perovskite absorber for tandem solar cells, Science (1979). 351 (2016). https://doi.org/10.1126/science.aad5845.

[38] J. Yang, Y. Chen, W. Tang, S. Wang, Q. Ma, Y. Wu, N. Yuan, J. Ding, W.H. Zhang, Crystallization tailoring of cesium/formamidinium double-cation perovskite for efficient and highly stable solar cells, Journal of Energy Chemistry. 48 (2020). https://doi.org/10.1016/j.jechem.2020.01.012.

[39] M. Saliba, T. Matsui, J.-Y. Seo, K. Domanski, J.-P. Correa-Baena, M. Khaja, S.M. Zakeeruddin, W. Tress, A. Abate, A. Hagfeldt, M. Grä, Cesium-containing triple cation perovskite solar cells: improved stability, reproducibility and high efficiency †, Cite This: Energy Environ. Sci. 9 (2016). https://doi.org/10.1039/c5ee03874j.

[40] F. Ünlü, E. Jung, J. Haddad, A. Kulkarni, S. Öz, H. Choi, T. Fischer, S. Chakraborty, T. Kirchartz, S. Mathur, Understanding the interplay of stability and efficiency in A-site engineered lead halide perovskites, APL Mater. 8 (2020). https://doi.org/10.1063/5.0011851.

[41] J. Sala, M. Heydarian, S. Lammar, Y. Abdulraheem, T. Aernouts, A. Hadipour, J. Poortmans, Compositional Investigation for Bandgap Engineering of Wide Bandgap Triple Cation Perovskite, (2021). https://doi.org/10.1021/acsaem.1c00810.
[42] N. Li, S. Tao, Y. Chen, X. Niu, C.K. Onwudinanti, C. Hu, Z. Qiu, Z. Xu, G. Zheng, L. Wang, Y. Zhang, L. Li, H. Liu, Y. Lun, J. Hong, X. Wang, Y. Liu, H. Xie, Y. Gao, Y. Bai, S. Yang, G. Brocks, Q. Chen, H. Zhou, Cation and anion immobilization through chemical bonding enhancement with fluorides for stable halide perovskite solar cells, Nat Energy. 4 (2019). https://doi.org/10.1038/s41560-019-0382-6.
[43] Y. Feng, Y. Zhang, C. Duan, M. Zhao, J. Dai, Optical properties of CsFAMA-based perovskite film and its application in the inverted solar cells with poly(methyl methacrylate) passivation layer, Opt Mater Express. 12 (2022) 3262. https://doi.org/10.1364/OME.463437.
[44] F. Ruf, M.F. Aygüler, N. Giesbrecht, B. Rendenbach, A. Magin, P. Docampo, H. Kalt, M. Hetterich, Temperature-dependent studies of exciton binding energy and phase-transition suppression in (Cs,FA,MA)Pb(I,Br) 3 perovskites, 7 (2019) 31113. https://doi.org/10.1063/1.5083792.
[45] T. Singh, T. Miyasaka, T. Singh, T. Miyasaka, CommuniCation Stabilizing the Efficiency Beyond 20% with a Mixed Cation Perovskite Solar Cell Fabricated in Ambient Air under Controlled Humidity, (2017). https://doi.org/10.1002/aenm.201700677.
[46] S. Ašmontas, A. Čerškus, J. Gradauskas, A. Grigucevičienė, K. Leinartas, A. Lučun, K. Petrauskas, A. Selskis, A. Sužiedėlis, E. Širmulis, R. Juškėnas, Cesium-containing triple cation perovskite solar cells, Coatings. 11 (2021) 1–12. https://doi.org/10.3390/coatings11030279.
[47] A. Kogo, Y. Sanehira, Y. Numata, M. Ikegami, T. Miyasaka, Amorphous Metal Oxide Blocking Layers for Highly Efficient Low-Temperature Brookite TiO 2-Based Perovskite Solar Cells, (2018). https://doi.org/10.1021/acsami.7b16662.
[48] Y. Wang, X. Liu, T. Zhang, X. Wang, M. Kan, J. Shi, Y. Zhao, The Role of Dimethylammonium Iodide in CsPbI 3 Perovskite Fabrication: Additive or Dopant? , Angewandte Chemie. 131 (2019). https://doi.org/10.1002/ange.201910800.
[49] Y. Zhang, G. Grancini, Y. Feng, A.M. Asiri, M.K. Nazeeruddin, Optimization of Stable Quasi-Cubic FA x MA 1−x PbI 3 Perovskite Structure for Solar Cells with Efficiency beyond 20%, 2 (2017) 24. https://doi.org/10.1021/acsenergylett.7b00112.
[50] J.J. Yoo, S. Wieghold, M.C. Sponseller, M.R. Chua, S.N. Bertram, N. Titan Putri Hartono, J.S. Tresback, E.C. Hansen, J.-P. Correa-Baena, V. Bulovic, T. Buonassisi, S. Sik Shin, M.G. Bawendi, An interface stabilized perovskite solar cell with high stabilized efficiency and low voltage loss †, 2192 | Energy Environ. Sci. 12 (2019) 2192. https://doi.org/10.1039/c9ee00751b.
[51] E.H. Jung, N.J. Jeon, E.Y. Park, C.S. Moon, T.J. Shin, T.Y. Yang, J.H. Noh, J. Seo, Efficient, stable and scalable perovskite solar cells using poly(3-hexylthiophene), Nature. 567 (2019). https://doi.org/10.1038/s41586-019-1036-3.
[52] N.J. Jeon, H. Na, E.H. Jung, T.Y. Yang, Y.G. Lee, G. Kim, H.W. Shin, S. il Seok, J. Lee, J. Seo, A fluorene-terminated hole-transporting material for highly efficient and stable perovskite solar cells, Nat Energy. 3 (2018). https://doi.org/10.1038/s41560-018-0200-6.

[53] N. Li, J. Liu, C. Li, Y. Li, J. Jia, Y. Wu, H. Yu, B. Yuan, B. Cao, Zwitterion-Stabilizing Scalable Bladed α-Phase Cs 0.1 FA 0.9 PbI 3 Films for Efficient Inverted Planar Perovskite Solar Cells, (2020). https://doi.org/10.1021/acssuschemeng.0c00417.
[54] S. Sun, T. Salim, N. Mathews, M. Duchamp, C. Boothroyd, G. Xing, T.C. Sum, Y.M. Lam, The origin of high efficiency in low-temperature solution-processable bilayer organometal halide hybrid solar cells, Energy Environ Sci. 7 (2014) 399–407. https://doi.org/10.1039/C3EE43161D.
[55] M. Aslam, T. Mahmood, A. Naeem, Organic Inorganic Perovskites: A Low-Cost-Efficient Photovoltaic Material, in: Perovskite and Piezoelectric Materials, 2021. https://doi.org/10.5772/intechopen.94104.
[56] T. Baikie, Y. Fang, J.M. Kadro, M. Schreyer, F. Wei, S.G. Mhaisalkar, M. Graetzel, T.J. White, Synthesis and crystal chemistry of the hybrid perovskite (CH 3NH3)PbI3 for solid-state sensitised solar cell applications, J Mater Chem A Mater. 1 (2013). https://doi.org/10.1039/c3ta10518k.
[57] M.A. Green, A. Ho-Baillie, H.J. Snaith, The emergence of perovskite solar cells, Nat Photonics. 8 (2014). https://doi.org/10.1038/nphoton.2014.134.
[58] M. Luan, J. Song, X. Wei, A.F. Chen, J. Liu, From chip-in-a-lab to lab-on-a-chip: towards a single handheld electronic system for multiple application-specific lab-on-a-chip (ASLOC), 18 (2014) 5257. https://doi.org/10.1039/c6ce00375c.
[59] I. Chung, B. Lee, J. He, R.P.H. Chang, M.G. Kanatzidis, All-solid-state dye-sensitized solar cells with high efficiency, (2012). https://doi.org/10.1038/nature11067.
[60] N. Islam, M. Yang, K. Zhu, Z. Fan, Mesoporous scaffolds based on TiO2 nanorods and nanoparticles for efficient hybrid perovskite solar cells, J Mater Chem A Mater. 3 (2015). https://doi.org/10.1039/c5ta06727h.
[61] W. Hu, W. Zhou, X. Lei, P. Zhou, M. Zhang, T. Chen, H. Zeng, J. Zhu, S. Dai, S. Yang, S. Yang, Low-Temperature In Situ Amino Functionalization of TiO 2 Nanoparticles Sharpens Electron Management Achieving over 21% Efficient Planar Perovskite Solar Cells, Advanced Materials. 31 (2019). https://doi.org/10.1002/adma.201806095.
[62] T. Leijtens, S.D. Stranks, G.E. Eperon, R. Lindblad, E.M.J. Johansson, I.J. McPherson, H. Rensmo, J.M. Ball, M.M. Lee, H.J. Snaith, Electronic properties of meso-superstructured and planar organometal halide perovskite films: Charge trapping, photodoping, and carrier mobility, ACS Nano. 8 (2014). https://doi.org/10.1021/nn502115k.
[63] A. Marchioro, J. Teuscher, D. Friedrich, M. Kunst, R. van de Krol, T. Moehl, M. Grätzel, J.E. Moser, Unravelling the mechanism of photoinduced charge transfer processes in lead iodide perovskite solar cells, Nat Photonics. 8 (2014). https://doi.org/10.1038/nphoton.2013.374.
[64] H. Zhang, M. Liu, W. Yang, L. Judin, T.I. Hukka, A. Priimagi, Z. Deng, P. Vivo, Thionation Enhances the Performance of Polymeric Dopant-Free Hole-Transporting Materials for Perovskite Solar Cells, Adv Mater Interfaces. 6 (2019). https://doi.org/10.1002/admi.201901036.
[65] J.-P. Correa-Baena, A. Abate, M. Saliba, W. Tress, T.J. Jacobsson, M. Grä, A. Hagfeldt, The rapid evolution of highly efficient perovskite solar cells, | Energy Environ. Sci. 10 (2017) 710. https://doi.org/10.1039/c6ee03397k.

[66] J. Zhang, B. Xu, L. Yang, C. Ruan, L. Wang, P. Liu, W. Zhang, N. Vlachopoulos, L. Kloo, G. Boschloo, L. Sun, A. Hagfeldt, E.M.J. Johansson, The Importance of Pendant Groups on Triphenylamine-Based Hole Transport Materials for Obtaining Perovskite Solar Cells with over 20% Efficiency, Adv Energy Mater. 8 (2018). https://doi.org/10.1002/aenm.201701209.
[67] S. Liu, X. Yi, H. Wang, T. Ye, K. Wang, W. Cao, J. Guan, R. Fan, Y. Yang, S. Hao, D. Xia, The Evolution of Classical Spiro-OMeTAD: Synthesis of Arylamine Endcapped Indenone Spirofluorene, Front Chem. 10 (2022). https://doi.org/10.3389/fchem.2022.898320.
[68] S. Li, Y.L. Cao, W.H. Li, Z.S. Bo, A brief review of hole transporting materials commonly used in perovskite solar cells, Rare Metals. 40 (2021) 2712–2729. https://doi.org/10.1007/s12598-020-01691-z.
[69] L. Canil, J. Salunke, Q. Wang, M. Liu, H. Köbler, M. Flatken, L. Gregori, D. Meggiolaro, D. Ricciarelli, F. de Angelis, M. Stolterfoht, D. Neher, A. Priimagi, P. Vivo, A. Abate, Halogen-Bonded Hole-Transport Material Suppresses Charge Recombination and Enhances Stability of Perovskite Solar Cells, Adv Energy Mater. 11 (2021). https://doi.org/10.1002/aenm.202101553.
[70] G. Wu, Y. Zhang, R. Kaneko, Y. Kojima, K. Sugawa, A. Islam, J. Otsuki, S. Liu, Triphenylamine-based hole transporting materials with thiophene-derived bridges for perovskite solar cells, Synth Met. 261 (2020). https://doi.org/10.1016/j.synthmet.2020.116323.
[71] P. Liu, B. Xu, Y. Hua, M. Cheng, K. Aitola, K. Sveinbjörnsson, J. Zhang, G. Boschloo, L. Sun, L. Kloo, Design, synthesis and application of a Π-conjugated, non-spiro molecular alternative as hole-transport material for highly efficient dye-sensitized solar cells and perovskite solar cells, J Power Sources. 344 (2017). https://doi.org/10.1016/j.jpowsour.2017.01.092.
[72] J. Zhang, B. Xu, M.B. Johansson, N. Vlachopoulos, G. Boschloo, L. Sun, E.M.J. Johansson, A. Hagfeldt, Strategy to Boost the Efficiency of Mixed-Ion Perovskite Solar Cells: Changing Geometry of the Hole Transporting Material, ACS Nano. 10 (2016). https://doi.org/10.1021/acsnano.6b02442.
[73] B. Xu, J. Zhang, Y. Hua, P. Liu, L. Wang, C. Ruan, Y. Li, G. Boschloo, E.M.J. Johansson, L. Kloo, A. Hagfeldt, A.K.Y. Jen, L. Sun, Tailor-Making Low-Cost Spiro[fluorene-9,9′-xanthene]-Based 3D Oligomers for Perovskite Solar Cells, Chem. 2 (2017). https://doi.org/10.1016/j.chempr.2017.03.011.
[74] Y. Hua, P. Liu, Y. Li, L. Sun, L. Kloo, Composite Hole-Transport Materials Based on a Metal-Organic Copper Complex and Spiro-OMeTAD for Efficient Perovskite Solar Cells, Solar RRL. 2 (2018). https://doi.org/10.1002/solr.201700073.
[75] L. Zhang, F. Yu, Q. Li, J. Su, J. Li, M. Li, Understanding interactions between halide perovskite surfaces and atmospheric/VOC gas molecules: An ab initio investigation, J Phys D Appl Phys. 51 (2018). https://doi.org/10.1088/1361-6463/aace7e.
[76] N.J. Jeon, H.G. Lee, Y.C. Kim, J. Seo, J.H. Noh, J. Lee, S. il Seok, O-methoxy substituents in spiro-OMeTAD for efficient inorganic-organic hybrid perovskite solar cells, J Am Chem Soc. 136 (2014). https://doi.org/10.1021/ja502824c.
[77] T. Zhang, I.E. Brumboiu, C. Grazioli, A. Guarnaccio, M. Coreno, M. de Simone, A. Santagata, H. Rensmo, B. Brena, V. Lanzilotto, C. Puglia, Lone-Pair Delocalization Effects within Electron Donor Molecules: The Case of Triphenylamine and Its

Thiophene-Analog, Journal of Physical Chemistry C. 122 (2018). https://doi.org/10.1021/acs.jpcc.8b06475.
[78] W. Shi, S. Fan, F. Huang, W. Yang, R. Liu, Y. Cao, Synthesis of novel triphenylamine-based conjugated polyelectrolytes and their application as hole-transport layers in polymeric light-emitting diodes, J Mater Chem. 16 (2006). https://doi.org/10.1039/b603704f.
[79] M. Thelakkat, Star-shaped, dendrimeric and polymeric triarylamines as photoconductors and hole transport materials for electro-optical applications, Macromol Mater Eng. 287 (2002). https://doi.org/10.1002/1439-2054(20020701)287:7<442::AID-MAME442>3.0.CO;2-H.
[80] P. Agarwala, D. Kabra, A review on triphenylamine (TPA) based organic hole transport materials (HTMs) for dye sensitized solar cells (DSSCs) and perovskite solar cells (PSCs): Evolution and molecular engineering, J Mater Chem A Mater. 5 (2017) 1348–1373. https://doi.org/10.1039/c6ta08449d.
[81] D.A. Magaldi-Lara, P.T. Toupance, K.M.-C.C. Cnrs, T. Rapporteur, F. Dumur, P.F. Goubard, T.-T. Bui, Synthesis of New Carbazole-based Hole Transport Molecules for Hybrid Perovskite Solar Cells Devant le jury composé de, 2019.
[82] S.N. Georgiades, P.G. Nicolaou, Recent advances in carbazole syntheses, in: Adv Heterocycl Chem, 2019. https://doi.org/10.1016/bs.aihch.2018.10.001.
[83] S. do Sung, M.S. Kang, I.T. Choi, H.M. Kim, H. Kim, M.P. Hong, H.K. Kim, W.I. Lee, 14.8% perovskite solar cells employing carbazole derivatives as hole transporting materials, Chemical Communications. 50 (2014). https://doi.org/10.1039/c4cc06716a.
[84] P. Gratia, A. Magomedov, T. Malinauskas, M. Daskeviciene, A. Abate, S. Ahmad, M. Grätzel, V. Getautis, M.K. Nazeeruddin, A Methoxydiphenylamine-Substituted Carbazole Twin Derivative: An Efficient Hole-Transporting Material for Perovskite Solar Cells, Angewandte Chemie - International Edition. 54 (2015). https://doi.org/10.1002/anie.201504666.
[85] L. Gao, T.H. Schloemer, F. Zhang, X. Chen, C. Xiao, K. Zhu, A. Sellinger, Carbazole-Based Hole-Transport Materials for High-Efficiency and Stable Perovskite Solar Cells, Cite This: ACS Appl. Energy Mater. 2020 (2020) 4492–4498. https://doi.org/10.1021/acsaem.0c00179.
[86] G. You, L. Li, S. Wang, J. Cao, L. Yao, W. Cai, Z. Zhou, K. Li, Z. Lin, H. Zhen, Q. Ling, Donor–Acceptor Type Polymer Bearing Carbazole Side Chain for Efficient Dopant-Free Perovskite Solar Cells, Adv Energy Mater. 12 (2022). https://doi.org/10.1002/aenm.202102697.
[87] A. Amat, E. Mosconi, E. Ronca, C. Quarti, P. Umari, M.K. Nazeeruddin, M. Grätzel, F. de Angelis, Cation-induced band-gap tuning in organohalide perovskites: Interplay of spin-orbit coupling and octahedra tilting, Nano Lett. 14 (2014). https://doi.org/10.1021/nl5012992.
[88] Z. Li, M. Yang, J.S. Park, S.H. Wei, J.J. Berry, K. Zhu, Stabilizing Perovskite Structures by Tuning Tolerance Factor: Formation of Formamidinium and Cesium Lead Iodide Solid-State Alloys, Chemistry of Materials. 28 (2016). https://doi.org/10.1021/acs.chemmater.5b04107.
[89] Y. Kawamura, H. Mashiyama, K. Hasebe, Structural Study on Cubic-Tetragonal Transition of CH3NH 3PbI3, J Physical Soc Japan. 71 (2002). https://doi.org/10.1143/JPSJ.71.1694.

[90] P.S. Whitfield, N. Herron, W.E. Guise, K. Page, Y.Q. Cheng, I. Milas, M.K. Crawford, Structures, Phase Transitions and Tricritical Behavior of the Hybrid Perovskite Methyl Ammonium Lead Iodide, Sci Rep. 6 (2016). https://doi.org/10.1038/srep35685.
[91] J.A. Christians, P.A. Miranda Herrera, P. v. Kamat, Transformation of the excited state and photovoltaic efficiency of CH3NH3PbI3 perovskite upon controlled exposure to humidified air, J Am Chem Soc. 137 (2015). https://doi.org/10.1021/ja511132a.
[92] H.T. Nguyen, S. Gerritsen, M.A. Mahmud, Y. Wu, Z. Cai, T. Truong, M. Tebyetekerwa, T. Duong, J. Peng, K. Weber, T.P. White, K. Catchpole, D. Macdonald, Tandem Solar Cells: Spatially and Spectrally Resolved Absorptivity: New Approach for Degradation Studies in Perovskite and Perovskite/Silicon Tandem Solar Cells (Adv. Energy Mater. 4/2020), Adv Energy Mater. 10 (2020). https://doi.org/10.1002/aenm.202070016.
[93] L. Nakka, Y. Cheng, A.G. Aberle, F. Lin, Analytical Review of Spiro-OMeTAD Hole Transport Materials: Paths Toward Stable and Efficient Perovskite Solar Cells, (2022). https://doi.org/10.1002/aesr.202200045.
[94] N. Ahn, K. Kwak, M.S. Jang, H. Yoon, B.Y. Lee, J.K. Lee, P. v. Pikhitsa, J. Byun, M. Choi, Trapped charge-driven degradation of perovskite solar cells, Nat Commun. 7 (2016). https://doi.org/10.1038/ncomms13422.
[95] S.N. Habisreutinger, T. Leijtens, G.E. Eperon, S.D. Stranks, R.J. Nicholas, H.J. Snaith, Carbon nanotube/polymer composites as a highly stable hole collection layer in perovskite solar cells, Nano Lett. 14 (2014). https://doi.org/10.1021/nl501982b.
[96] J. Yang, B.D. Siempelkamp, D. Liu, T.L. Kelly, Investigation of CH3NH3PbI3degradation rates and mechanisms in controlled humidity environments using in situ techniques, ACS Nano. 9 (2015). https://doi.org/10.1021/nn506864k.
[97] G. Niu, W. Li, F. Meng, L. Wang, H. Dong, Y. Qiu, Study on the stability of CH3NH3PbI3 films and the effect of post-modification by aluminum oxide in all-solid-state hybrid solar cells, J Mater Chem A Mater. 2 (2014). https://doi.org/10.1039/c3ta13606j.
[98] M.M. Lee, J. Teuscher, T. Miyasaka, T.N. Murakami, H.J. Snaith, Efficient hybrid solar cells based on meso-superstructured organometal halide perovskites, Science (1979). 338 (2012). https://doi.org/10.1126/science.1228604.
[99] K. Aitola, K. Domanski, J.P. Correa-Baena, K. Sveinbjörnsson, M. Saliba, A. Abate, M. Grätzel, E. Kauppinen, E.M.J. Johansson, W. Tress, A. Hagfeldt, G. Boschloo, High Temperature-Stable Perovskite Solar Cell Based on Low-Cost Carbon Nanotube Hole Contact, Advanced Materials. 29 (2017). https://doi.org/10.1002/adma.201606398.
[100] Z. Hawash, L.K. Ono, S.R. Raga, M. v. Lee, Y. Qi, Air-exposure induced dopant redistribution and energy level shifts in spin-coated Spiro-Meotad films, Chemistry of Materials. 27 (2015). https://doi.org/10.1021/cm504022q.
[101] Y. Fang, X. Wang, Q. Wang, J. Huang, T. Wu, Impact of annealing on spiro-OMeTAD and corresponding solid-state dye sensitized solar cells, Physica Status Solidi (A) Applications and Materials Science. 211 (2014). https://doi.org/10.1002/pssa.201431366.

[102] H.J. Snaith, M. Grätzel, Enhanced charge mobility in a molecular hole transporter via addition of redox inactive ionic dopant: Implication to dye-sensitized solar cells, Appl Phys Lett. 89 (2006). https://doi.org/10.1063/1.2424552.
[103] Z. Song, C.L. Mcelvany, A.B. Phillips, I. Celik, P.W. Krantz, S.C. Watthage, G.K. Liyanage, D. Apul, M.J. Heben, A technoeconomic analysis of perovskite solar module manufacturing with low-cost materials and techniques †, Energy Environ. Sci. 10 (2017) 1297. https://doi.org/10.1039/c7ee00757d.
[104] L. Meng, J. You, Y. Yang, Addressing the stability issue of perovskite solar cells for commercial applications, Nat Commun. 9 (2018). https://doi.org/10.1038/s41467-018-07255-1.
[105] Y. Tachibana, K. Umekita, Y. Otsuka, S. Kuwabata, Performance improvement of CdS quantum dots sensitized TiO2 solar cells by introducing a dense TiO2 blocking layer, J Phys D Appl Phys. 41 (2008). https://doi.org/10.1088/0022-3727/41/10/102002.
[106] T. bin Song, Q. Chen, H. Zhou, C. Jiang, H.H. Wang, Y.M. Yang, Y. Liu, J. You, Y. Yang, Perovskite solar cells: Film formation and properties, J Mater Chem A Mater. 3 (2015) 9032–9050. https://doi.org/10.1039/c4ta05246c.
[107] R. Li, M. Liu, S.K. Matta, A. Hiltunen, Z. Deng, C. Wang, Z. Dai, S.P. Russo, P. Vivo, H. Zhang, Sulfonated Dopant-Free Hole-Transport Material Promotes Interfacial Charge Transfer Dynamics for Highly Stable Perovskite Solar Cells, Adv Sustain Syst. 5 (2021). https://doi.org/10.1002/adsu.202100244.
[108] N. Cai, F. Li, Y. Chen, R. Luo, T. Hu, F. Lin, S.M. Yiu, D. Liu, D. Lei, Z. Zhu, A.K.Y. Jen, Synergistical Dipole–Dipole Interaction Induced Self-Assembly of Phenoxazine-Based Hole-Transporting Materials for Efficient and Stable Inverted Perovskite Solar Cells, Angewandte Chemie - International Edition. 60 (2021). https://doi.org/10.1002/anie.202107020.
[109] Y.C. Chen, Y.P. Lin, T.E. Hsieh, M.W. Huang, Preparation of Cu(In,Ga)Se2 nanoparticles via solvothermal method in conjunction with ball milling process and its applications to thin-film solar cells, J Alloys Compd. 791 (2019). https://doi.org/10.1016/j.jallcom.2019.03.253.
[110] M.R. Cavallari, G. dos Santos, F.J. Fonseca, Nanoelectronics, Nanoscience and Its Applications. (2017) 35–69. https://doi.org/10.1016/B978-0-323-49780-0.00002-8.
[111] C. Zhang, S. Wu, L. Tao, G.M. Arumugam, C. Liu, Z. Wang, S. Zhu, Y. Yang, J. Lin, X. Liu, R.E.I. Schropp, Y. Mai, Fabrication Strategy for Efficient 2D/3D Perovskite Solar Cells Enabled by Diffusion Passivation and Strain Compensation, Adv Energy Mater. 10 (2020). https://doi.org/10.1002/aenm.202002004.
[112] A. Erbe, S. Nayak, Y.H. Chen, F. Niu, M. Pander, S. Tecklenburg, C. Toparli, How to probe structure, kinetics, and dynamics at complex interfaces in situ and operando by optical spectroscopy, in: Encyclopedia of Interfacial Chemistry: Surface Science and Electrochemistry, 2018. https://doi.org/10.1016/B978-0-12-409547-2.14061-2.